

19990126 073

***IR&T***

***Innovative Research & Technology***

***SBIR Phase I R&D Contract Phase I Report***

***Contract # DASG60-98-M-0122***

***Sparse Array Radiometric Imaging (SARI)***

***using an Electronic Mirror***

**SPONSORED BY**

**BMDO Innovative Science and Technology Office**

**MANAGED BY**

**U.S. Army and Missile Defense Command**

Contract Start Date : 4/29/98

Contract End date: 12/31/98

Reporting Period 4/29/98 - 12/31/98

Principal Investigator: Dr. W.A. Peebles (310) 399-2423

The views and conclusions contained in this document are those of the authors and should not be interpreted as necessarily representing the official policies, either expressed or implied, of the Government.

Distribution: Approved for public release; distribution is unlimited

326 25th St., Santa Monica, California 90402.

Tel./FAX (310) 399-2423

# REPORT DOCUMENTATION PAGE

Form Approved  
OMB No. 0704-0188

Public reporting burden for this collection of information is estimated to average 1 hour per response, including the time for reviewing instructions, searching existing data sources, gathering and maintaining the data needed, and completing and reviewing the collection of information. Send comments regarding this burden estimate or any other aspect of this collection of information, including suggestions for reducing this burden, to Washington Headquarters Services, Directorate for Information Operations and Reports, 1215 Jefferson Davis Highway, Suite 1204, Arlington, VA 22202-4302, and to the Office of Management and Budget, Paperwork Reduction Project (0704-0188), Washington, DC 20503.

1. AGENCY USE ONLY (Leave Blank)		2. REPORT DATE 12/31/98		3. REPORT TYPE AND DATES COVERED FINAL REPORT 4/29/98 - 12/31/98	
4. TITLE AND SUBTITLE Sparse Array Radiometric Imaging using an Electronic Mirror				5. FUNDING NUMBERS Contract DASG60-98-M-0122	
6. AUTHOR(S) DR. W.A. Peebles					
7. PERFORMING ORGANIZATION NAME(S) AND ADDRESS(ES) Innovative Research & Technology, IR&T, 326 25th St., Santa Monica, CA 90402				8. PERFORMING ORGANIZATION REPORT NUMBER IRT 101	
9. SPONSORING/MONITORING AGENCY NAME(S) AND ADDRESS(ES) BMDO Innovative Science & Technology Office, 7100 Defense, Pentagon, Rm. 1E167, Washington D.C. 20301-7100				10. SPONSORING/MONITORING AGENCY REPORT NUMBER	
11. SUPPLEMENTARY NOTES					
12a. DISTRIBUTION/AVAILABILITY STATEMENT Approved for public release Distribution is unlimited.				12b. DISTRIBUTION CODE	
13. ABSTRACT (Maximum 200 words)  All-weather, covert, millimeter-wave surveillance deployed on unmanned aerial vehicles (UAVs) would offer a new, highly desirable capability for a wide range of both military and commercial applications. Conventional focal plane imaging systems have failed to provide such a capability with adequate spatial resolution to make deployment attractive. Increasing antenna aperture through conventional sparse-aperture synthesis, as utilized in radio astronomy, has also failed due to the required number of antenna elements and the associated weight and power loads. IR&T has proposed a radical, new concept - beam-steerable, sparse aperture, interferometric imaging. In this concept IR&T has significantly reduced the total number of required antenna elements (and thereby the associated power, weight, computational load, etc.) while maintaining image resolution and field of regard (FOR). This is achieved through the introduction of "electronic mirrors" to synchronously steer fewer but larger individual antennae elements. The electronic mirror adds the necessary sophistication for successful application to a wide range of surveillance conditions.					
14. SUBJECT TERMS Millimeter-wave, all-weather, radiometric imaging, sparse array, interferometry				15. NUMBER OF PAGES 30	
				16. PRICE CODE	
17. SECURITY CLASSIFICATION OF REPORT Unclassified	18. SECURITY CLASSIFICATION OF THIS PAGE Unclassified	19. SECURITY CLASSIFICATION OF ABSTRACT Unclassified	20. LIMITATION OF ABSTRACT UL		

# **Sparse Array Radiometric Imaging (SARI) using an Electronic Mirror**

## **CONTENTS**

<b>REPORT DOCUMENTATION PAGE</b>	<b>1</b>
<b>TABLE OF CONTENTS</b>	<b>2</b>
<b>1. INTRODUCTION</b>	<b>3</b>
<b>2. THE PROPOSED INNOVATION</b>	<b>6</b>
2.1 Summary of Passive Imaging	6
2.2 The Proposed Innovation	20
2.3 Summary of Phase I Results	27
2.4 References	29
<b>3. PHASE I RESULTS</b>	<b>31</b>
3.1 Introduction	31
3.2 Phase I Technical Objectives & Results	31
Task 1 Results	31
Task 2 Results	57
3.3 Conclusions	79
3.4 References	80

## **BMDO/SBIR Phase I Final Report**

**Contract DASG60-98-M-0122**

# **Sparse Array Radiometric Imaging (SARI) using an Electronic Mirror**

## ***1. Introduction***

The utilization of solid-state microwave technology for military, commercial and research applications has experienced tremendous growth over the last two decades. For example, microwave components have been integrated into systems for communications, radar, remote sensing, navigation, surveillance, electronic warfare, radiometers, medicine, plasma research, astronomy, nondestructive testing, etc. However, the many advantages of operating at higher, millimeter-wave frequencies (e.g. improved spatial resolution, increased bandwidth, more compact, lightweight systems) have not been fully realized due primarily to technological limitations at these frequencies combined with increasing cost and decreasing reliability. For example, in many applications transmitter and receiver systems often require an *electronic beam-steering capability*. Conventionally, this is achieved by the application of a phased antenna array. Phased arrays typically employ *active* solid-state circuits at the antennae (often with MMIC architecture) in order to provide the required amplitude and phase control. This approach becomes increasingly difficult to implement as frequencies increase into the millimeter-wave region. For example, the RF losses associated with microstrip coupling to the antennae become large. The mechanical fabrication process also becomes increasingly challenging with the overall result that the final system becomes extremely complex, costly and potentially unreliable.

These technological constraints have therefore limited deployment of millimeter-wave systems in a variety of areas. For example, development and deployment on an uninhabited aerial vehicle (UAV) of a *passive, all-weather, high-resolution, radiometric imaging surveillance* system dictates operation at W-band or possibly higher frequencies in order to achieve acceptable resolution. To date, such a system has been unavailable even though it would

provide an unmatched passive imaging capability through obscurants such as rain, cloud, dust, smoke and sand.

The work performed during this SBIR Phase I Contract has established feasibility of a radical new concept - *beam-steerable, sparse aperture, interferometric imaging*. This concept has the potential to revolutionize all-weather, surveillance capabilities. The practical realization of such a system depends on the demonstration of an "electronic mirror" (a low-loss, electronically controllable, millimeter-wave beam-steering element) which has the effect of fundamentally modifying the scaling of interferometer/sparse aperture imaging systems. The Phase I Program has identified a potential *low-cost solution to realization of the electronic mirror*. The solution is based on quasi-optical, monolithic solid state diode arrays, where thousands of diodes are monolithically integrated together with their antenna into a 2-D planar array. Electronic biasing of rows of diodes creates a variable impedance surface which then controls the reflected phase of an incident electromagnetic wave thereby resulting in voltage controlled beam-steering. During the Phase I Program, analysis of the optimum diode structure combined with preliminary design has provided increased confidence in the practicality of the "electronic mirror". In addition, analysis of the beam-steerable, sparse aperture interferometric imaging concept has served to illustrate the power, flexibility and breadth of application offered by such a system.

In summary, the Phase I Program has determined the following:

- (1) Unequivocally established the practical feasibility of the radical new concept of a "beam-steerable, sparse aperture, radiometric imaging system". *IR&T now has total confidence that successful implementation of the concept will result in a previously unattainable all-weather, passive (or covert) imaging capability suitable for deployment from a platform such as a UAV.*
- (2) Realization of such a system is dependent on the availability of an "electronic mirror". The mirror provides the necessary control to vary the FOR (field of regard) as well as providing the flexibility to optimize image acquisition and quality in a varying military environment. *Work performed during Phase I indicates that monolithic diode arrays are best-suited to satisfy these technical requirements.*

A full prototype demonstration is essential prior to deployment. This demonstration will therefore form the focus of the follow-on **Phase II Program**. *It is planned to design, fabricate and establish performance characteristics of large aperture (3 inch) diode arrays through extensive test. The resultant "electronic mirror" will be utilized in a 94GHz radiometric imaging system to fully demonstrate the beam-steering capability.* In addition, through close collaboration with and support from General Atomics - a privately held company that manufactures the Predator - it is planned to generate a detailed design for a beam-steerable, sparse-array all-weather imaging system that would be fully integrated into the Predator UAV. A Phase III Program would subsequently be pursued whose goal would be a full-test of this all-weather imaging system on a UAV.

(3) As the Phase I Program evolved the *breadth of application for both active and passive beam-steerable, all-weather, millimeter wave imaging systems has dramatically expanded*. Application areas include: all-weather surveillance, covert night-time navigation, covert warning of bad weather ahead, covert weapons detection, covert surveillance through walls, all-weather target identification and designation from a UAV, imaging through smoke, non-destructive testing, etc. It should be noted that many of these applications have dual-use in both military and civilian environments. This indicates that successful development would lead to broad applicability with the potential for large markets driven primarily by unit cost. This clearly indicates that detailed attention has to be directed towards cost reduction and high reliability during Phase II. This, of course, is fully consistent with the diode array concept.

(4) The Phase I activity has led to *consolidation of fruitful collaboration with General Atomics Co.* (manufacturer of the Predator UAV). Collaboration will be essential to future system development and commercialization. In addition to the current BMDO SBIR Phase I activity, ongoing collaboration in the millimeter-wave area includes development of an all-weather, active targeting and designating system deployed on a UAV. A contract is now in place after a successful response to a DARPA BAA (Note this effort does not involve direct demonstration of the electronic mirror). *The proposed BMDO/SBIR Phase II Program will include continued close involvement with General Atomics including financial support in the form of matching funds*

The results of the **Phase I Program** have established feasibility and strongly endorse fabrication and test of a large aperture electronic mirror together with a demonstration of beam-steerable radiometric imaging during the follow-on **Phase II Program**. A successful follow-on **Phase II Program** will bring to reality a new, covert, all-weather, surveillance system which, together with existing capabilities, will significantly benefit the modern military. In addition, such a capability (since it presents no health hazard) has a wide range of commercial applications ranging from unmanned surveillance (geological, weather, oil, etc) to marine navigation, fire fighting, weapon detection, non-destructive testing, etc. Close collaboration with **General Atomics** ensures financial and marketing support for a wide range of anticipated Phase III commercialization projects.

## **2. *The Proposed Innovation***

Prior to describing the principles of the proposed innovation, let us first summarize the existing status of passive or covert imaging.

### **2.1 Summary of Passive Imaging**

#### **2.1.1 *Introduction.***

The advantages of operating surveillance and communication systems at high millimeter-wave frequencies include compactness, low weight, improved resolution and lower observability or "stealthiness". Many of these advantages are important for the majority of military as well as many commercial applications. Additional issues that factor into the choice of operating frequency are cost and reliability. When the cost of a surveillance or communication system becomes a significant portion of the cost of the carrier clearly there is resistance to implementation. The existing status of high-frequency millimeter-wave radiation sources and components, such as steerable antennae, is that in order to achieve the required performance characteristics the cost becomes excessive and the reliability less than desired. For example, in the case of a phased array antenna, an array of separate individual active solid-state circuits is employed, often with MMIC architecture, in order to provide the necessary amplitude and phase control. As frequencies increase this becomes more and more difficult to implement in an efficient and reliable manner. For example, the RF losses associated with stripline and microstrip

coupling increase dramatically with frequency and become prohibitive in F-band (90-140 GHz). In addition, the mechanical fabrication requirements also become increasingly challenging with the overall result that the final system becomes extremely complex, costly and potentially unreliable. This existing technological approach is therefore currently limited to lower millimeter-wave frequencies. *IR&T* believes that the full benefits of higher frequency operation will only be achieved through a quasi-optical circuit approach. High power sources can be developed through quasi-optical spatial combining in planar arrays, and low-loss propagation through quasi-optical transmission in overmoded guide or free-space. As described in later Sections quasi-optical monolithic diode arrays can also be utilized to generate a variable impedance surface, which can serve as a low-cost efficient beam-steering component at high millimeter-wave frequencies.

Despite some of the limitations of existing technology the attractiveness of passive radiometric imaging at millimeter-wave frequencies has been pursued for a number of years in a few narrow application areas: all-weather aircraft landing/take-off (2.1, 2.2), and personal weapon detection (2.3, 2.4). It should be noted that these efforts have focussed on applications operating at relatively short distance or range. Let us consider some of the advantages and difficulties associated with imaging at millimeter-wave frequencies.

Visible or optical imaging sensors have, of course, been available for more than 100 years. Image resolution in good weather is excellent, but there are obvious drawbacks related to night-time and bad weather operation, as well as the inability of visible light to transmit through a wide range of materials. Advances in infrared technology in the last 50 years have eliminated our inability to "see in the dark". Night vision goggles are now routinely utilized in *both* military and commercial environments. The millimeter-wave spectrum offers a further enhancement in surveillance capability that would enable us to see through cloud, smoke, as well as a wide range of materials such as clothing, camouflage, foliage and even building materials.

The millimeter-wave spectrum lies between 30 and 300 GHz and historically has received little attention in regard to passive imaging. The reasons for this are three-fold:

- (1) reduced resolution in the millimeter-wave region due to relatively long wavelength operation



- (2) weak natural emission at these frequencies and
- (3) technological limitations alluded to previously.

It should be noted that in reference to (2), although the radiation intensity of a 300°K black body peaks in the infrared, this situation is changed dramatically when the effect of absorption in the atmosphere caused, for example, by fog is included in the assessment (see Fig. 2.1).

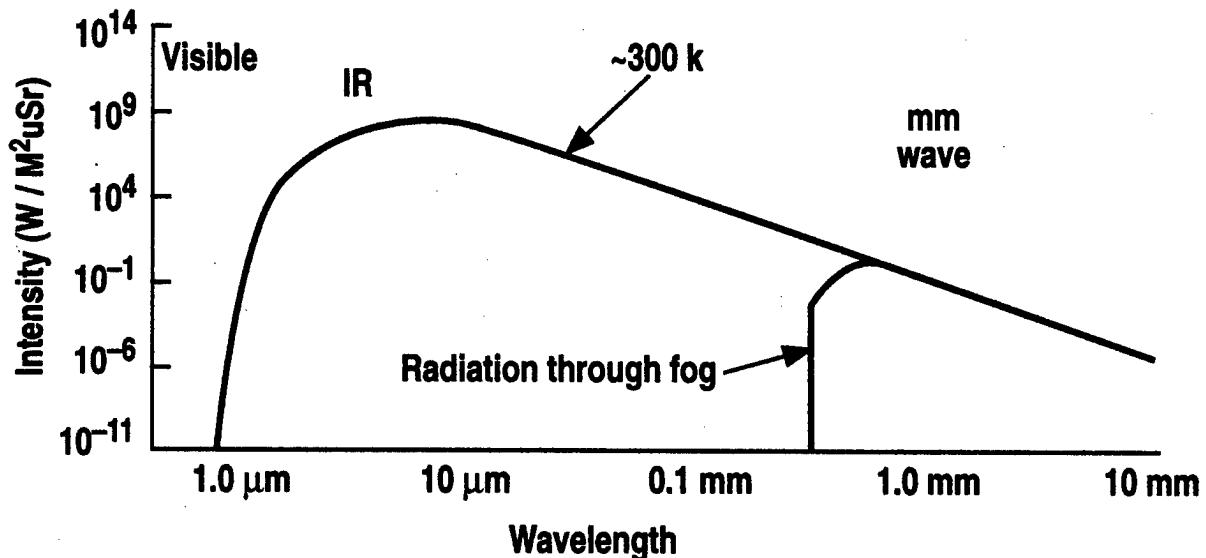


**Figure 2.1** Transmission of various wavelengths through clear atmosphere and fog.

As can be seen, in this situation, the propagated signal actually peaks in the millimeter wave spectral region. This is in fact one of the major reasons why imaging in the millimeter wave region is so attractive and should be seriously investigated. It represents the "last frontier" of the electromagnetic spectrum and offers an all-weather imaging capability that complements alternative systems in the visible and infrared spectral regions. The current SBIR contract addresses the remaining concerns related to imaging at millimeter-wave frequencies: spatial resolution and technology cost. Through implementation of a beam-steerable, sparse-array large-aperture antenna at frequencies ~ 94GHz high-resolution images can be obtained over a suitable field of view. The electronic mirror, realized through electronic control of the surface impedance of a GaAs wafer, satisfies many of the concerns regarding technological limitations and cost. Monolithic fabrication techniques eliminate discrete components, reduce rf losses and bring low-cost millimeter-wave beam-steering to the market. In addition to the proposed innovations other

technological advances in recent years, such as low-noise millimeter-wave amplifiers, active multipliers and MMIC systems in general serve to make this the optimum time to successfully develop high-resolution, all-weather, millimeter-wave imaging systems.

From the perspective of military surveillance there is an additional advantage related to the millimeter-wave spectral region. The emissivity  $\epsilon$  of an object relates to its ability to absorb electromagnetic radiation. An emissivity of unity indicates that the object or material is a perfect *absorber* whereas an emissivity of zero indicates a perfect *reflector*. The emissivity is dependent on wavelength, polarization, surface roughness, material properties, etc. In a situation where surveillance of an outdoor scene from a UAV is being performed the, so-called, radiometric temperature of the scene is based on factors such as: *emission* from the scene components, *reflection* of the sky radiation by the scene, *propagation* through the atmosphere, etc. In this regard there are significant differences between viewing a scene in the millimeter-wave rather than the infrared spectral region. For example, the emissivity of a painted metal tank is very low in the millimeter-wave region but quite large in the infrared i.e. the tank strongly reflects the sky radiation in the millimeter-wave region but acts like an absorber in the infrared. However, the ground on which the tank sits is a strong absorber in both spectral regions i.e. the emissivity is large. In this situation the image contrast would be far greater in the millimeter-wave region than in the infrared, thus causing the tank to stand out strongly relative to its surroundings. In addition, if the tank was operating and the engine was "hot", thereby increasing emission, contrast would increase somewhat in the infrared. However, the millimeter-wave image contrast would be largely independent of whether the tank engine was operating or not. In other words the infrared image is dependent on actual temperature differences between the tank and background, whereas the millimeter-wave image relies more on emissivity differences between objects with contrast resulting from reflection of the sky radiation. Another advantage of the millimeter-wave spectral region relates to propagation through the atmosphere, which is far better in the millimeter-wave spectral region thereby allowing good imaging through cloud, fog, smoke, etc.

Finally propagation through camouflage, clothing, etc. represents another distinct advantage. During the Phase I Program *IR&T* has performed some transmission measurements in the spectral region from 60 to 100 GHz to demonstrate the potential of imaging through

various materials. Transmission is good through cotton, plastics, camouflage netting, etc. This advantage is illustrated in **Fig. 2.2** where a millimeter-wave image of a Ford truck is shown. Note that the millimeter-wave image has no difficulty maintaining image quality even though camouflage netting covers the front cab portion of the truck.

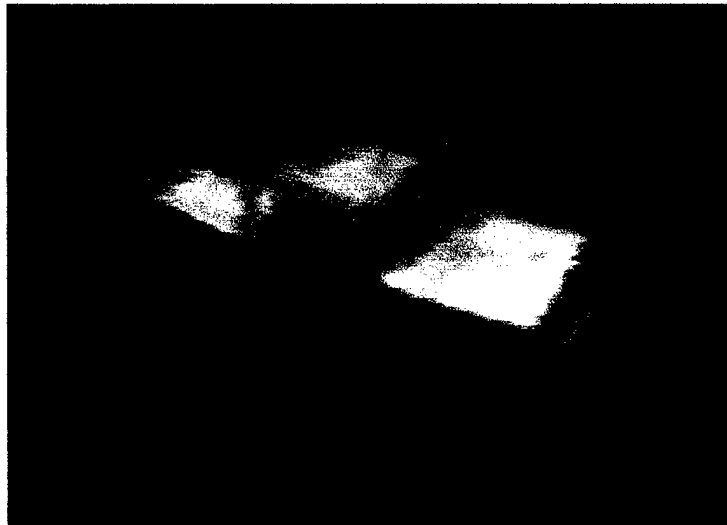


**Figure 2.2** Millimeter-wave (94 GHz) image of a Ford truck obtained by mechanical scanning of a single receiver system. Note that the image is easily interpreted and has similarities to visible and infrared images. However, in contrast with visible or infrared the camouflage netting has little effect on image quality in the mm-wave region. Contrast is achieved by reflection of the cold sky temperature and not the actual “temperature” of the truck – image quality is independent of whether the truck is operating or not. Image obtained through collaborative effort of **IR&T** and **General Atomics** (manufacturer of Predator UAV)

### **2.1.2 Examples of Millimeter-wave Radiometric Imaging.**

A group at the **Jet Propulsion Laboratory** led by **W.J. Wilson** performed one of the earliest (1986) demonstrations of millimeter-wave, all-weather imaging surveillance (**Ref. 2.5**). A passive 3mm (98GHz) radiometer was fabricated and near-real-time images were produced using a mechanically scanned antenna mounted to a commercial helicopter. A schematic illustrating the concept is shown in **Fig 2.3**. The antenna aperture was only ~17 inches and so angular resolution was limited by diffraction to ~ 0.5 degrees. A lightweight flat reflector was mechanically scanned cross-track  $\pm 20$  degrees at a 4Hz rate. A two-axis scanner, controlled by a microcomputer with inputs from both rate and angle gyros, was used to scan the reflector and to correct for aircraft movement due to turbulence. The two-axis scanner also utilized a butterfly

scanning pattern to compensate for the forward aircraft motion to produce a linear raster scan on the ground. Altitudes of  $\sim 2500$  ft (800m) were typically employed resulting in a spatial image resolution of only 20ft (6m). Higher altitudes would have resulted in further degradation of image resolution. This relatively poor resolution was a direct result of the antenna aperture size. The radiometer consisted of a local oscillator (Gunn diode) pumped waveguide mixer followed by a series of low-noise amplifiers. An intermediate frequency of 3GHz was selected with a filter width of  $\sim 2$  GHz. Typical double sideband noise temperatures of  $\sim 1000^\circ\text{K}$  at 98GHz were achieved. **Figure 2.4** illustrates a typical image obtained with this system while flying over Carlsbad, California. The images (visible and mm-wave) were taken on a cloudy, rainy day at an altitude of 1800ft. The layer of broken clouds completely obscured the ground scene in the visible image, whereas the ability of the mm-wave imager to penetrate the clouds is clearly demonstrated. In the mm-wave image, the freeways, vehicles, parking lots and buildings appear as colder targets reflecting the sky radiation. The image illustrates the contrast in emissivity between ground, concrete and metal.

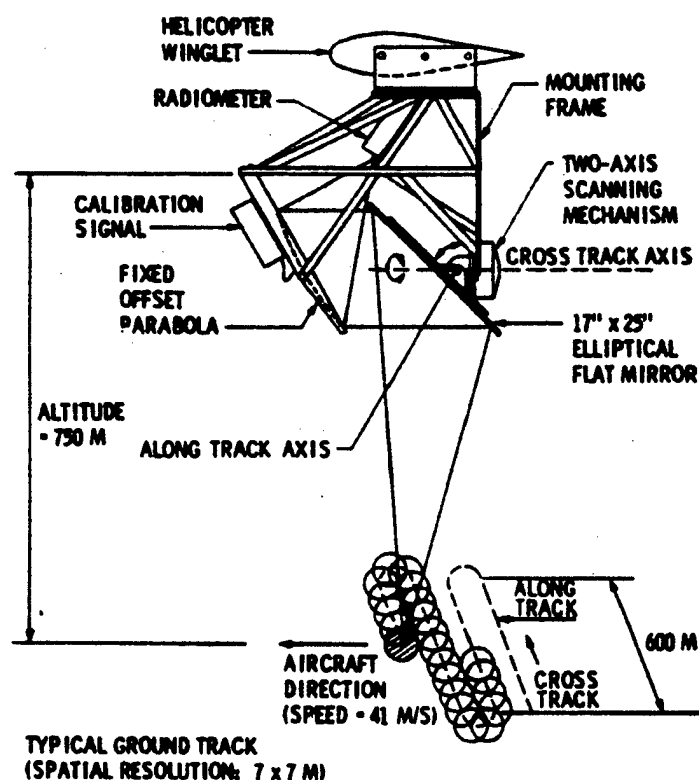


**Figure 2.3** System configuration for scanning radiometric imaging system utilized by Wilson et al. (Ref. 2.5). The system was attached to the winglet of a Bell Jet Ranger helicopter.



**Figure 2.4** Visible and millimeter-wave images taken by Wilson *et al.*(Ref. 2.5) over Carlsbad, California during a cloudy day. Note that the mm-wave images easily penetrate the cloud cover.

For many years the work of Wilson et al. remained state-of-the-art. The basic advantages of millimeter-wave radiometric imaging had been demonstrated. However, the work also served to illustrate the major disadvantage: poor spatial resolution limited by the relatively small antenna dimension to wavelength ratio.

Work began to focus around development of an imaging capability that would allow aircraft to take off, land, and taxi in fog and low cloud ceiling. This has long been a high priority for both military and commercial aviation. In this situation range to the landing strip was relatively short and so adequate spatial resolution was possible using millimeter-wave systems. Technology had also advanced to a point where a new approach to radiometric imaging could be undertaken and the concept of a millimeter-wave camera came into existence primarily through work led by TRW (2.1) who had developed low-noise 94 GHz amplifiers (2.6). These W-band amplifiers allow the more complicated mixer/local oscillator combination of Wilson to be eliminated and replaced by a series of amplifiers followed by filters and detectors – *heterodyne* detection was therefore replaced by *direct amplification and detection*. The current TRW concept consists of a two-dimensional staring focal-plane array operating at 94 GHz. An array of W-band amplifiers/detectors is placed in the focal or image plane of a 24 inch diameter lens. This is conceptually identical to a video camera with an optical lens and CCD array. Spatial resolution is again limited by the antenna aperture and operating wavelength.

Following the work of TRW, the Thermotrex Corporation (San Diego) also pursued a variety of short range applications (2.2, 2.3, 2.7). However, their concept differed considerably from that of TRW and is illustrated in **Figure 2.5**. Their patented architecture combines a phased array receiver with an acousto-optic (or electro-optic) processor to create a real-time millimeter-wave-to-visible light converter. A slotted waveguide staring antenna with periodic couplers along its length detects radiation from an elevation angle that is a function of signal frequency. Broadband thermal emission can therefore be spectrally analyzed to map out intensity versus elevation angle. A phased array of such antenna elements adds azimuth directionality through phase analysis. A mulitchannel acousto-optic modulator reverses the frequency vs elevation angle and phase vs azimuth angle relationships of the antenna to deflect laser light into a visible replica of the mm-wave radiation striking the antenna. An ordinary CCD camera is then utilized to record the wavelength-converted image. It has been suggested that the Thermotrex

approach could significantly lower costs in comparison with the approach suggested by TRW. However, the final cost for these systems are not yet established.

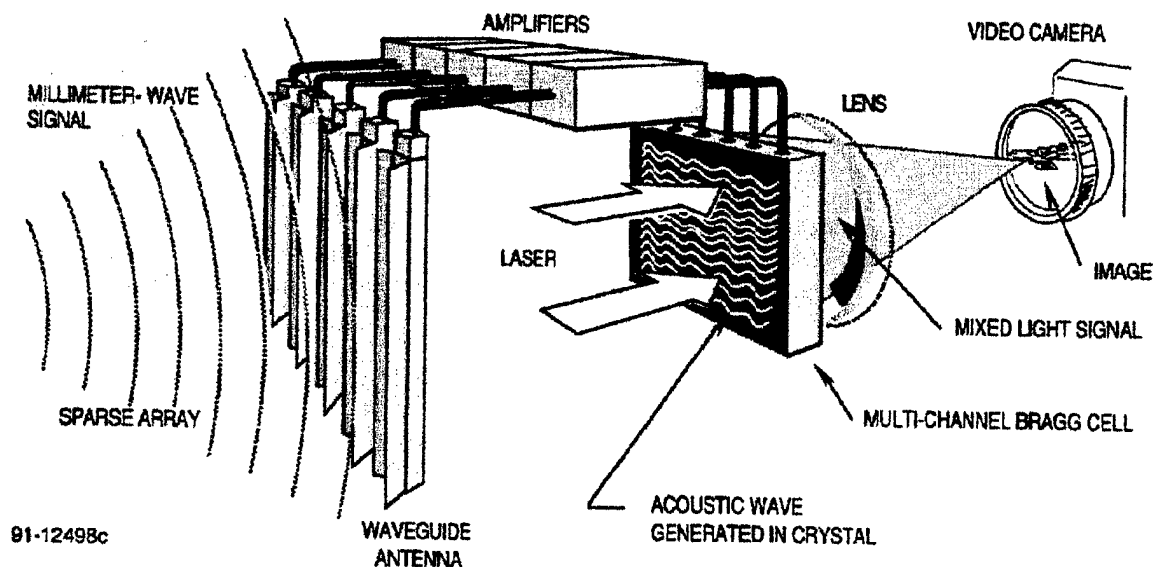


**Figure 2.5** Schematic illustrating Thermotrex approach to mm-wave imaging. After Lovberg et al. (Refs. 2.2, 2.7).

The Thermotrex Group, as illustrated in **Figures 2.6 and 2.7**, have demonstrated the image quality and range of potential short range applications of mm-wave imaging (2.2, 2.3, 2.7). **Figure 2.6** illustrates a series of warehouses and roads at a range of 300 to 700 meters. The coldest temperatures are displayed as white and the warmest temperatures as black. Note that several of the warehouse roofs appear less white, indicating that they are manufactured from

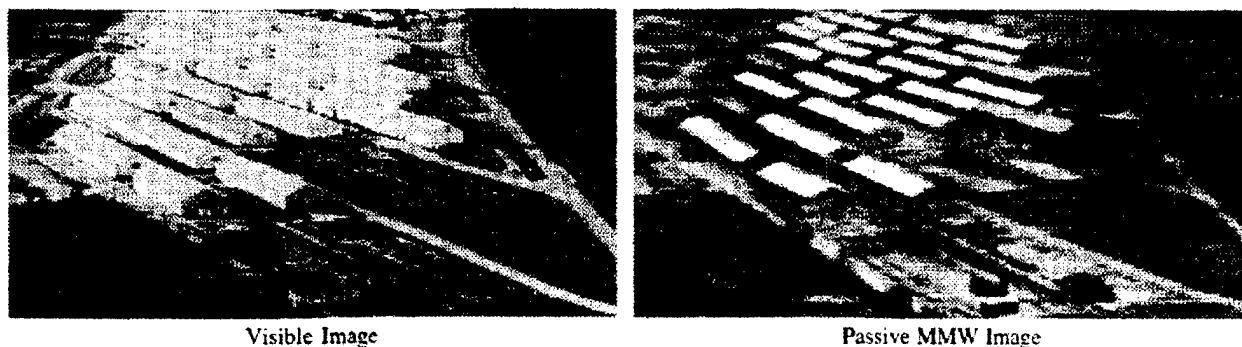
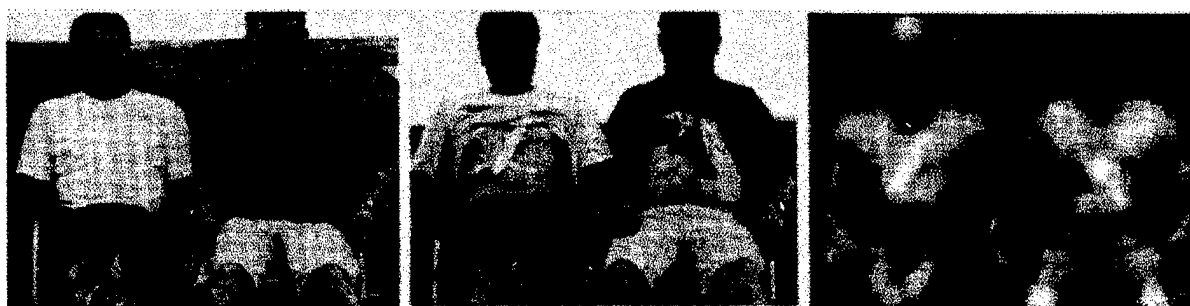


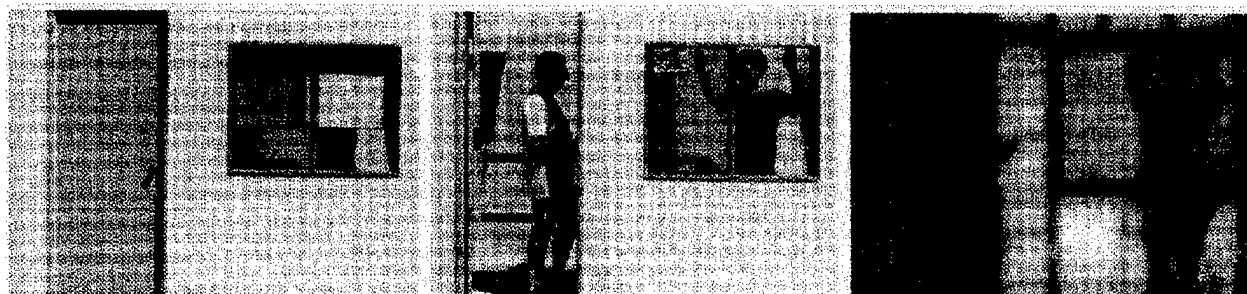
**Figure 2.6.** Visible and mm-wave images using Thermotrex "camera". After Lovberg et al (Refs. 2.2, 2.3, 2.7)

non-metallic materials which reflect less of the cold sky. This again indicates that the mm-wave image represents an “emissivity” image and actually provides new and sometimes important information to complement other sensor data.

**Figure 2.7** illustrates two other interesting visible and mm-wave images. First, **Fig. 2.7a** illustrates an image of two people sitting outdoors wearing concealed weapons under their shirts. Note that the mm-wave image appears to reveal body contours due to the low-loss transmission through clothing. The hidden knife and gun are easily identified in the mm-wave image.



(a)



(b)

**Figure 2.7 a** Visible and mm-wave images of concealed weapon detection  
**b.** Visible and mm-wave images taken through wood, sheet-rock, glass and window shade. After Lovberg et al. (Refs. 2.2, 2.3, 2.7).

It should be noted that the image was taken outdoors to ensure that the cool sky reflection from the metal objects was maximized. Lower contrast would be obtained indoors under normal conditions. The second image serves to indicate that several building materials transmit mm-wave radiation. The mm-wave image was taken through wood, sheet-rock, glass and window shade. However, the “lighting” for this image was not natural. A large wall of metal was tilted at a 45 degrees angle to reflect the cold temperature of the overhead sky. The image therefore is more demonstrative of the ability of mm-waves to penetrate a wide range of material rather than



a “real” image. Note that images created outdoors for UAV surveillance do not suffer from this drawback. Indoor images will require some form of artificial enhancement as illustrated in Fig. 2.7b which may well be acceptable for detection of concealed weapons and explosives.

The TRW and Thermotrex concepts potentially satisfy applications, such as airborne take-off and landing, where the range is small. However, in surveillance scenarios related to satellite, UAV or airborne missions it is clear that ranges of many kilometers are more appropriate. In this situation a focal plane array is totally impractical. Using an aperture of 60 cm diameter (it is difficult to imagine a much larger aperture due to weight and packaging constraints) an angular resolution (given approximately by  $\lambda/d$ ) of  $\sim 0.3$  degrees is to be expected. At an altitude of 3 kilometers this translates into an image resolution of 15m. Clearly for the majority of needs this is inadequate. In order to develop a millimeter-wave, radiometric imaging surveillance capability it is clear that much larger aperture antennae have to be utilized.

The need to increase antenna aperture, especially for a UAV, naturally leads to an approach based on that adopted by the radio-astronomy community many years ago – that of interferometric imaging or sparse array synthesis. Sparse aperture synthesis was first developed at microwave frequencies in the 1950's and has since become a standard astronomical imaging technique (Refs 2.8, 2.9). The resolution of an imaging system depends on the range of wavenumbers, or components of the Fourier spectrum of the scene, which are collected. A classical imaging system collects all wavenumbers which are intercepted by the main aperture. Such a filled aperture system provides multiply redundant measurements of all measured wavenumbers. The sparse aperture approach proceeds from the realization that image spatial resolution can be maintained in a system with much less total collecting area, so long as the complete set of wavenumbers is still collected, i.e. the redundancy of the wavenumber measurements is dramatically reduced by thinning out the number of receivers in the collection aperture. This approach preserves image spatial resolution, but system sensitivity is lost as the collection area has decreased as compared with a filled aperture. Overall, however, the sparse array approach reduces system cost, complexity, power draw, weight and computational load, and provides the only practical approach to the realization of large aperture mm-wave imaging systems for airborne applications. This is the approach adopted – and improved on – by *IR&T*.

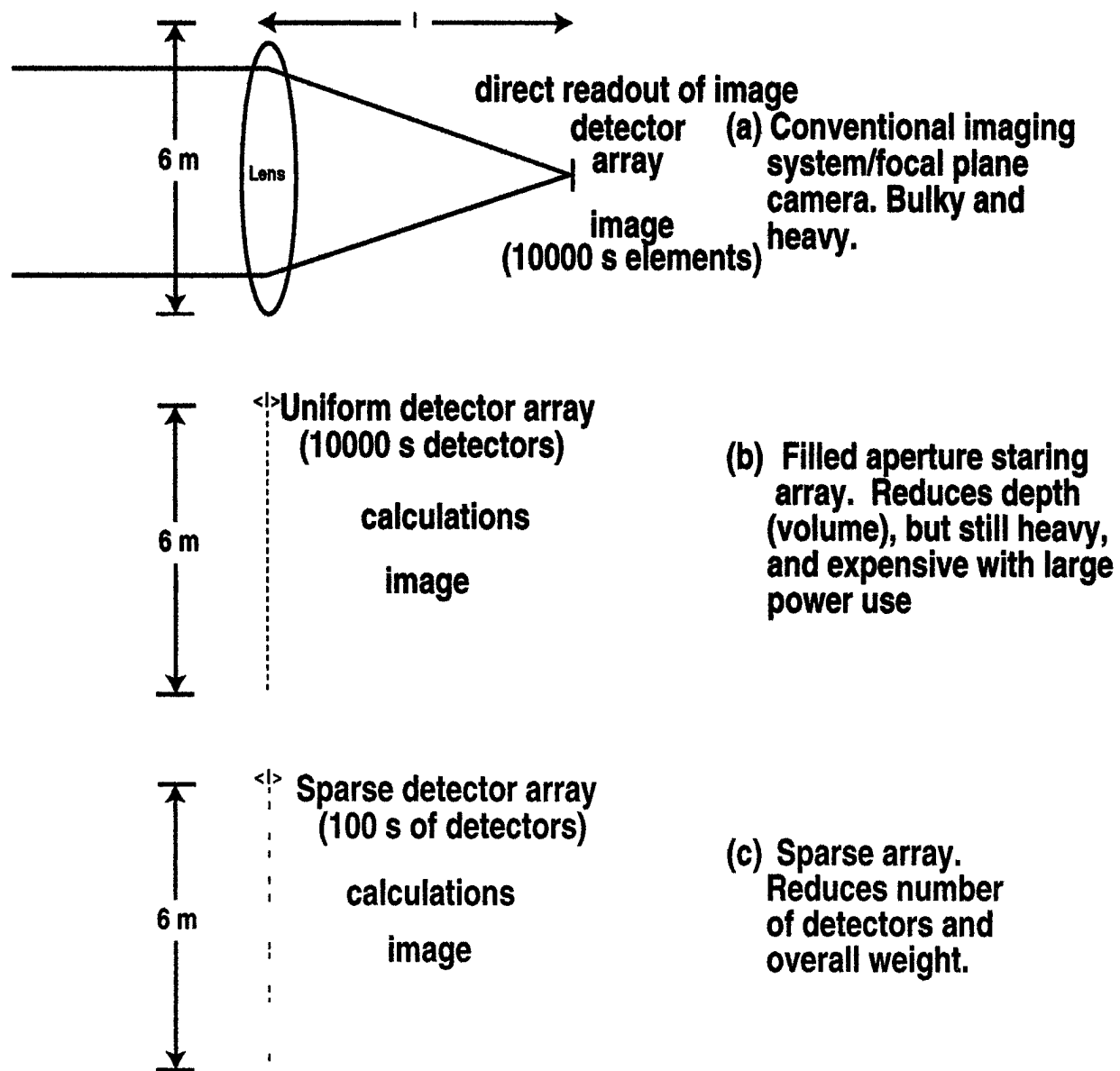


**Figure 2.8.** Schematic illustration of the three main approaches to realizing a mm-wave imaging system. (a) A conventional imaging system/focal plane camera. This corresponds to the approach utilized in the TRW imaging camera, and in the JPL system. (b) A filled aperture staring array. This corresponds to the approach adopted in the Thermotrex imaging system. As compared with (a), a staring array saves considerably on volume. (c) A sparse array – same geometry as (b), but with far fewer receivers in the array. The “sparseness” of the array reduces system cost, complexity, power draw, weight and computational load.

The three main approaches to realizing a mm-wave imaging system discussed above are shown schematically in **Fig. 2.8**. A conventional imaging system/focal plane camera, as illustrated in **Fig. 2.8(a)**, corresponds to the approach utilized in the TRW imaging camera and also in the JPL system. A filled aperture staring array, **Fig. 2.8(b)**, corresponds to the approach adopted in the Thermotrex imaging system, where the main aperture is now uniformly sampled, and the image is reconstructed electronically. A sparse array, **Fig. 2.8(c)**, has the same geometry as a filled staring array, but with far fewer receivers in the array. **Figure 2.9** illustrates the difference in how images are formed as between the synthesis approach used with a sparse array, and a mechanically scanned radiometer as flown by JPL. Implementation of such sparse arrays is discussed in more detail in Sections. 2.2.1 and 3.2.1 below.

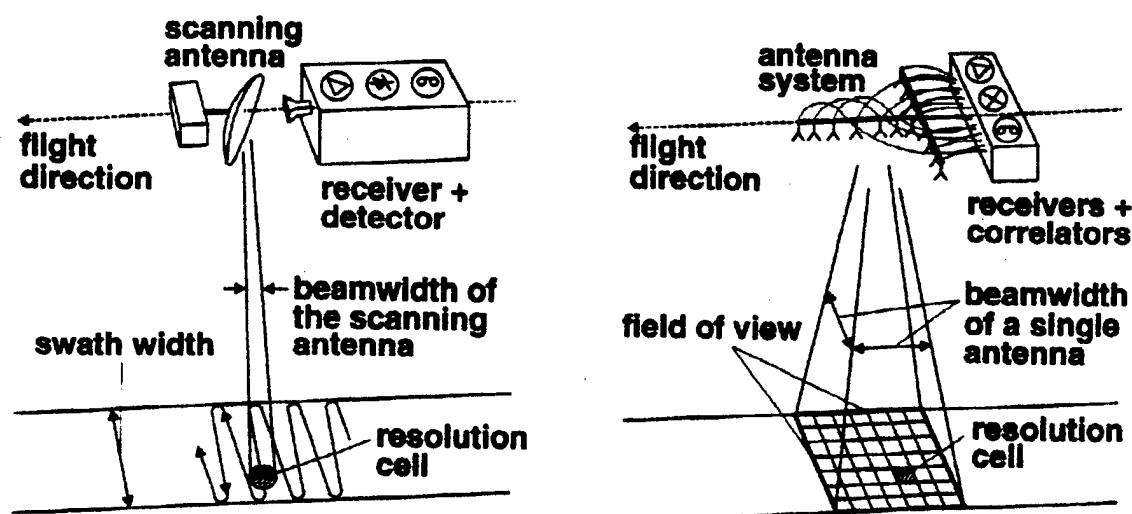


**Figure 2.9.** Schematic illustration of the difference in image formation as between a conventional imaging system with a mechanically scanned aperture, (as used by JPL, Ref. 2.5) and an interferometric/sparse aperture synthesis approach. *Figure after Ref. 2.10.*

Finally, it is important to note that sparse array images have been successfully obtained in terrestrial applications (in addition to the common use of the technique for astronomical imaging). **Figure 2.10** shows a mm-wave image obtained using a demonstration sparse aperture interferometric imaging system implemented by the DLR Institute in Germany, **Ref. 2.10**. All the main features present in the visible image can be seen in the mm-wave sparse aperture image. The background clutter in the mm-wave image is due to amplifier drifts over the time taken to

move the single detector used in the measurements – this would not be present in a production system using a receiver array.

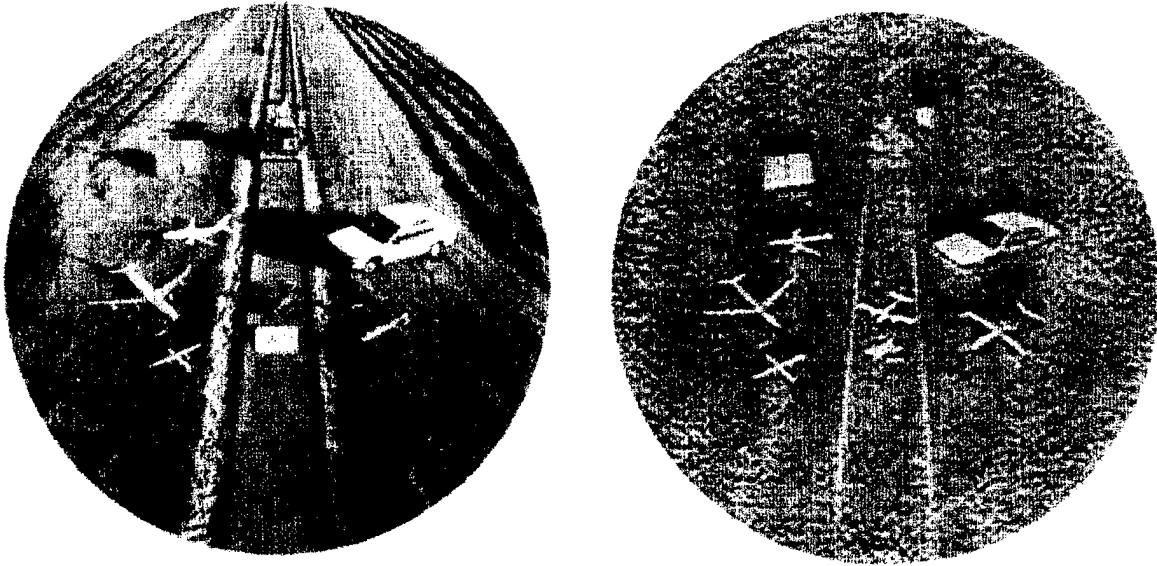


**Figure 2.10.** Example of a mm-wave (37 GHz) sparse aperture image from a ground based demonstration system (on right). A corresponding visual image is shown on the left. The background clutter visible in the mm-wave image is due to amplifier drifts which would not be present in a production system. *Figure after Ref. 2.10.*

## 2.2 The Proposed Innovation

### 2.2.1 *Technical Basis for Beam-steerable Sparse Aperture Imaging*

*IR&T* has developed an innovative solution to the problem of adequate field of regard, temperature sensitivity, and spatial resolution in a mm-wave sensor, while keeping the number of detector elements and thus power, weight and complexity low. The solution to the problem has two major elements:

1. **Significant reduction in the required number of individual elements of the sparse aperture array through the use of larger individual antenna elements.** This leads to reduced weight, power and computational complexity, thereby enabling for the first time a practical design of an imaging radiometric surveillance system. However, the field of regard (FOR) is reduced by the large antenna apertures used.
2. **Recovery of the full Field of Regard (FOR) with minimal loss in image quality through the use of electronic mirror elements.** Importantly, the electronic mirrors allow **control of the imaging properties** based on the weather or tactical conditions that exist at any particular time. The electronic mirror adds the sophistication necessary for successful application to a wide range of surveillance conditions.

The principal components of the *IR&T* approach are illustrated schematically in **Fig. 2.11**.

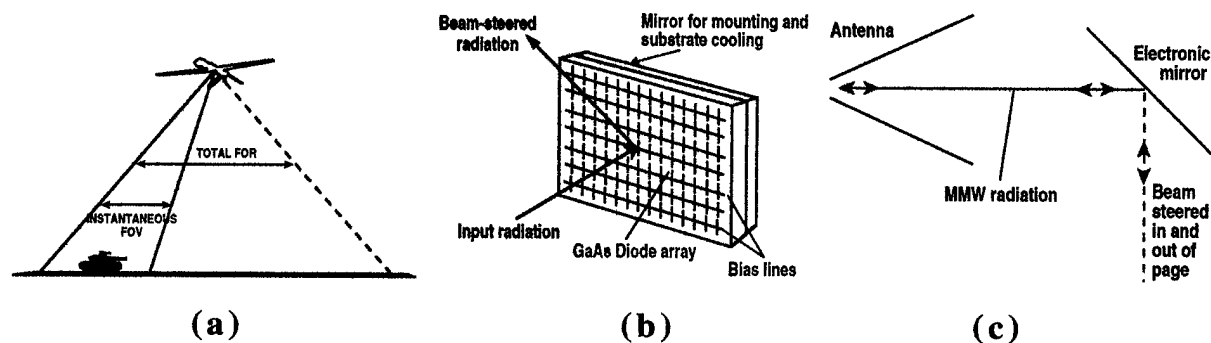


**Figure. 2.11.** *Principal components of the IR&T approach: (a) Imaging radiometer mounted on UAV, illustrating small instantaneous FOR together with larger total FOR obtained by using electronic mirrors for beam steering. (b) Realization of electronic mirror using monolithic beam-steering diode array fabricated on GaAs. (c) Schematic of receiver element utilizing the electronic mirror for beam steering.*

The proposed *IR&T* approach contains *two* levels of beam-steering/synthesis: within the instantaneous FOR of the individual antenna elements, standard interferometric imaging/sparse aperture techniques are used, while electronic beam steering implemented via adjustable electronic mirrors is used to scan the instantaneous FOR across the desired total FOR. As compared with a conventional approach, in the *IR&T* system the number of receiver/antenna elements (which governs the cost and complexity of the system) is reduced, while the total receiver area (which is low-cost and does not affect system complexity) is increased. The proposed new approach has several major advantages:

1. Order of magnitude fewer components reduces cost, complexity, power, weight and computing requirements to acceptable levels.
2. Reduced instantaneous FOR eliminates the grating lobe problem that can affect conventional interferometric/sparse array systems. With the reduced instantaneous FOR it is also no longer necessary to have a minimum detector spacing of  $\lambda/2$ , but rather a spacing of 1/2 the antenna dimension
3. The reduced instantaneous FOR, combined with relatively large fill factor, leads to good synthesized beam properties, i.e. acceptable point spread function (PSF), low side lobe levels, etc.
4. The smaller instantaneous FOR in the *IR&T* design significantly reduces the problem of rf bandwidth limitation as compared with a conventional sparse aperture design. In a conventional interferometric synthesis system the rf bandwidth B is limited to small values by the need to keep the frequency variation of propagation distance induced phase shifts small compared to the primary phase shifts due to the varying angular positions of the targets.

A very successful and widely adopted solution to obtaining large aperture imaging systems was developed by the radio astronomy community in the 1950's — interferometric imaging, also known as sparse aperture synthesis (Refs.2.8, 2.9). In this approach a distributed set of small antennas (diameter d) are used to synthesize the spatial resolution of a much larger antenna with a baseline equal to the maximum separation between individual antenna elements (baseline diameter D). Using this technique, the astronomy community has constructed synthetic aperture imaging systems with baselines varying from 100's of meters to thousands of kilometers. With

an interferometric/sparse aperture system the spatial resolution obtained is the same as that which would be obtained by a filled aperture of the same diameter  $D$ , but the temperature sensitivity is degraded ( $\Delta T$  increased) by a fill factor. The fill factor is defined as the ratio of the area of a filled array of diameter  $D$  to the total receiving area of the sparse array,  $D^2/Nd^2$ . Explicitly, the temperature sensitivity of a filled aperture radiometer system is given by

$$\Delta T = \frac{T_{sys}}{\sqrt{B\tau}}, \quad (1)$$

where  $T_{sys}$  is the receiver system noise temperature,  $B$  the receiver rf bandwidth, and  $\tau$  is the receiver integration time, while the temperature sensitivity of a sparse array system is

$$\Delta T = \frac{D^2}{Nd^2} \frac{T_{sys}}{\sqrt{B\tau}}, \quad (2)$$

where  $N$  is the number of antennas within the sparse array, and typically the fill factor  $D^2/Nd^2 \gg 1$ . In astronomy, the fill factor induced sensitivity degradation in interferometric systems is not that important since very long observation times can be used to compensate. For earth observation systems, however, the maximum integration time is severely limited, and the fill factor has a major impact on system design, for example in the design of a proposed synthetic aperture radiometer system for deployment on a NASA earth observation satellite, the 1.4 GHz ESTAR system (Refs. 2.11, 2.12).

A radiometric surveillance system has to meet three major requirements simultaneously:

- (1) In order to provide image contrast, adequate temperature sensitivity (small  $\Delta T$ ) is required to allow discrimination between the thermal emission levels of the various objects within the radiometer field of regard. The required temperature sensitivity depends on the nature of the targets to be imaged, i.e. metal targets have a larger temperature contrast than terrain, etc. Typically  $\Delta T$  is of the order of 1–5 K for ground targets.
- (2) Adequate spatial resolution — 1-2 m is desirable, corresponding approximately to National Image Interpretability Rating Scale (NIIRS) resolution levels 4-5.
- (3) Adequate field of regard (FOR) — a field of regard leading to an imaged swath width of several kilometers on the ground is desired.

To date, it has proved impossible to *simultaneously* meet typical requirements in a mm-wave sparse aperture system for surveillance applications. The reason for this is that obtaining a wide instantaneous FOR at mm-wavelengths requires the use of small antenna elements (~mm diameter), which for apertures of more than a few meters implies that *thousands* of antenna/receiver systems are necessary in order to maintain an acceptable temperature sensitivity and avoid the appearance of grating lobes within the FOR. Thus, mm-wave sparse-aperture systems considered to date have been impractical on the grounds of cost, weight, power and computational load (the number of computations needed to construct an image scales as the *square* of the number of antenna elements). Consequently, for space/airborne applications “conventional” interferometric techniques are essentially limited to microwave frequencies, as in the proposed NASA ESTAR system (Refs. 2.11, 2.12). As already described at the start of this section, the *IR&T* approach specifically addresses and solves these problems.

Standard expressions, such as Eq. (2) above, do not transparently show the inter-relationship between operational requirements, such as target range and required total field of regard, and system performance parameters such as the temperature sensitivity. In the following expression we have substituted for the maximum possible integration time in Eq. (2), making allowance for multiple measurements of the same pixel, and for the need to scan the instantaneous FOR in the proposed *IR&T* approach. This results in a single expression that is applicable to both the conventional and *IR&T* approaches:

$$\Delta T = T_{\text{sys}} \frac{D^2}{NR\lambda^2} \theta_r^{3/2} \sqrt{\frac{v}{Bh}}, \quad (3)$$

where  $R = d/d_0$ ,  $d_0 = \lambda/\theta_r$ ,  $\theta_r$  is the required *total* sensor system field of regard in radians,  $v$  is the sensor system velocity relative to the target,  $h$  is the range to the target (~ UAV altitude), and the other parameters are as defined earlier –  $d$  is the diameter of the individual antennas comprising the array,  $D$  is the diameter of the array (array baseline),  $T_{\text{sys}}$  is the receiver system noise temperature, and  $B$  the receiver rf bandwidth. The temperature resolution of Eq. 3 is obtained with a spatial resolution ( $\Delta x$ ) at the target of  $\Delta x \sim \lambda h/D$ . Equation 3 illustrates the many possibilities for parameter tradeoffs present in radiometric imaging system design, a flexibility considerably enhanced by the new parameter  $R$  discussed next.



The difference between the proposed *IR&T* system and conventional approaches arises in the parameter  $R$ . In conventional synthetic aperture systems the diameter of the antenna elements  $d$  is at most equal to  $d_0$ , the diameter which would result in an instantaneous field of regard equal to the required total sensor system FOR, i.e. in a conventional system  $R \sim 1$ . In the proposed *IR&T* approach,  $d$  is chosen much larger than  $d_0$ , such that  $R \gg 1$ . As can be seen from Eq. (2), leaving all other parameters on the right hand side the same, an increase in  $R$  leads to improved (smaller) temperature sensitivity. Thus the electronically scanned *IR&T* approach changes the system scaling such that there is a net improvement in system performance. In reality, the approach taken would be to design a system for a particular  $\Delta T$ , and utilize the performance improvement represented by  $R > 1$  to decrease the number of antenna elements  $N$ , which is the major driver in system cost, power and computational load. For example, using  $R = 10$ , which is quite practical, the number of antenna elements required to obtain a particular  $\Delta T$  is reduced by an order of magnitude. Thus, by changing the system performance scaling the *IR&T* approach enables a practical mm-wave large diameter (multi-meter) synthetic aperture design. *An increase of an order of magnitude in aperture diameter compared with previous filled aperture/focal plane imaging designs (Refs. 2.1, 2.2) is now practical.*

### 2.2.2 Technical Basis for an "Electronic" Mirror

As described above the "electronic mirror" is an essential component necessary to simultaneously realize an all-weather surveillance capability on a UAV. Electronic beam-steering, which, for example, allows radars to track many targets simultaneously, is relatively straightforward at microwave frequencies. Extension to higher millimeter-wave frequencies, where bandwidth and resolution improve and spatial size shrinks, has proven extremely difficult and costly. However, *IR&T* believes that the concept of utilizing monolithic, solid-state varactor diode arrays for electronically controlled beam steering offers a reliable, low-cost approach whose time has come (see Fig 2.12). A periodic metal grid on a GaAs wafer is monolithically loaded with varactor diodes. The incident electromagnetic wave reflects from the array surface. The phase of the reflected wave can then be controlled everywhere on the array through suitable biasing of the varactor diodes. *The electromagnetic wave is steered through the progressive phase shift created across the array. The electronically applied bias modifies the reactance, which controls the reflected phase.* The concept is illustrated conceptually below in Fig. 2.12.

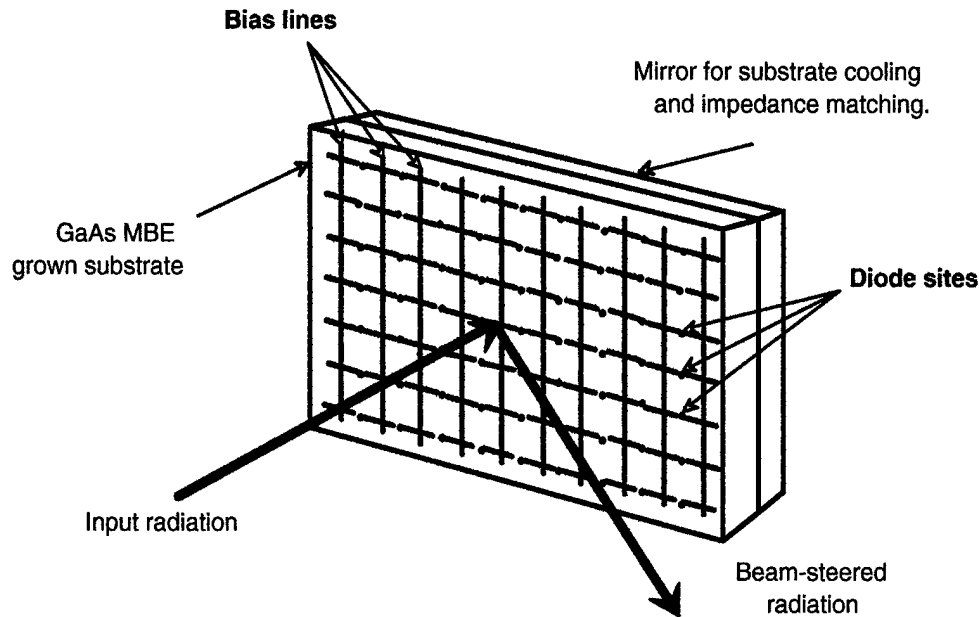


**Figure 2.12** Schematic illustrating concept of beam-steering array. Non-linear varactor diodes are monolithically integrated with antennas and bias lines on a GaAs wafer to produce a variable impedance surface. The bias lines allow introduction of a progressive phase shift across the array surface that can be utilized for beam-steering and focusing.

The concept of utilizing monolithic, solid-state diode arrays for electronically controlled beam steering initiated at Cal. Tech. by Prof. David Rutledge with the thesis of **W.W. Lam (Ref. 2.13)**. The work of **Lam (Ref. 2.13)** demonstrated that the diode array concept was capable of varying the phase of a reflected electromagnetic wave; a  $70^\circ$  phase shift was demonstrated at 93 GHz. However, this pioneering work did not demonstrate the projected beam steering and focusing properties. The more recent thesis work of **L.B. Sjogren** at UCLA expanded on Lam's initial work and provided a limited demonstration of a wide range of control capabilities that included beam steering, beam focusing, amplitude modulation/switching as well as polarization control (**Ref. 2.14**). **Figure 2.13** illustrates the beam steering achieved with Sjogren's array. As can be seen, angular steering of  $\sim \pm 6^\circ$  was achieved in this proof-of-concept experiment where the array was biased simply in two halves. The small angular steering obtained in this work was a direct result of the relatively small phase shift achieved across the array ( $\sim 60^\circ$ ).

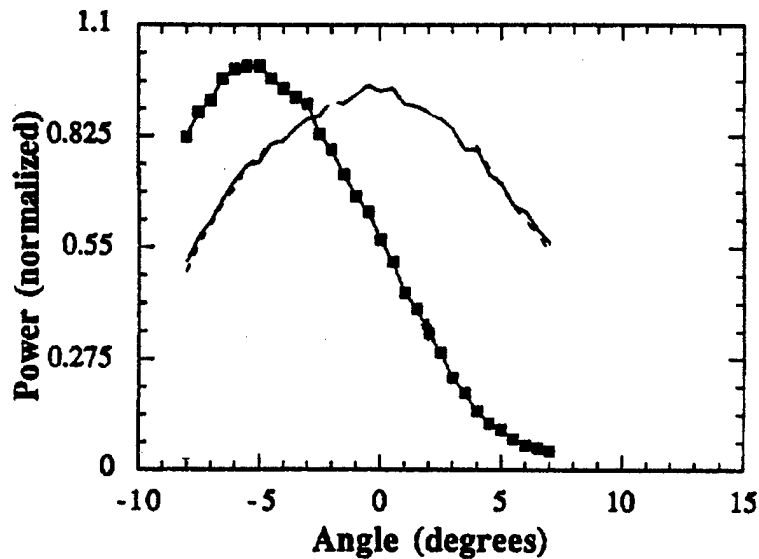


**Figure 2.13.** Beam steering results of Sjogren et al. (Ref. 2.14). E-plane power patterns for beam steering at 116.6 GHz are illustrated for two different applied bias voltages.

*IR&T* proposes to develop *quasi-optical, monolithic solid-state array technology* as an innovative, reliable, cost-effective solution. Planar, monolithic arrays of non-linear diodes integrated with associated antennae and bias circuitry are proposed for electronic beam-steering. A full prototype demonstration (Phase II) would lead to worldwide commercialization in a variety of commercial and military applications, since there exist a number of advantages over conventional technology :

- (1) Monolithic diode arrays can be fabricated at *low-cost*. This is particularly true for beam steering arrays, when compared to the alternative of providing individual phase/amplitude control.
- (2) Monolithic arrays can be fabricated using simple solid-state processing techniques which leads to reliable operation at high-frequencies. *IR&T* has already fabricated and tested monolithic diode arrays for millimeter-wave source applications under a NASA Phase II SBIR Contract. A monolithic array of BNN diodes was utilized as a tripler to produce record CW output powers at 180 GHz. The system operated reliably and suffered no damage even though illuminated with Watt-level input powers. Monolithic fabrication leads to low-cost, reliable and reproducible components.

- (3) The array concept also offers *exceptional flexibility*. For example, the same beam-steering diode array can be utilized as a variable phase shifter to correct phase errors, as a focusing element or for amplitude modulation.
- (4) Monolithic multiplier arrays also offer the significant advantage of *graceful degradation*. Damage to individual diodes in the monolithic array result in a minimal reduction in overall performance properties of the array.

**Section 3** will describe *IR&T's* plans for realization of a practical electronic mirror suitable for implementation in sparse array imaging system suitable for all-weather, surveillance on a UAV.

### 2.3 Summary of Phase I Results.

The primary thrust of the proposed **Phase I Program** was to establish feasibility of a millimeter-wave, interferometric imaging concept that utilizes emerging "electronic mirror" technology. The **Phase I Program** has fully established feasibility for the radical new concept of a beam-steerable sparse aperture interferometric surveillance system suitable for deployment on a UAV. In addition, the realization of the electronic mirror through the concept of a monolithic varactor diode array has been investigated and preliminary design successfully completed. The proposed Technical Objectives of the **Phase I Program** are reproduced below:

The prime technical goals for the **Phase I Program** were:

**Technical Objective 1.** Perform detailed design study for a thinned interferometric passive millimeter wave imaging system. The order of magnitude improvement in system weight and complexity provided by the electronic mirror will be the basis for the design. Particular attention will be given to optimizing the total system size, weight, and detector number, for specified target range and required temperature and spatial resolution. Attention will be also paid to the PSF of the synthesized beam, and sidelobe minimization. Design studies will be performed for three candidate system applications: a low flying (6500 ft) Predator UAV system, a high flying (60,000 ft) UAV/plane system, and an orbiting satellite system. Alternate deployment platforms and mission for the design study can also be specified by the funding authority.

**Technical Objective 2.** Perform the detailed engineering design of the optimum diode element for the monolithic beam-steering array. The MBE doping specifications required for the optimum anti-series varactor diode will be determined and fabrication process identified. In addition, the masks will be designed for a beam-steering array operating at 94 GHz to produce a scan capability of  $\pm 30^\circ$ .

**Technical Objective 3.** Generate a detailed **Final Report** documenting the results and conclusions of the **Phase I Program**.

The above tasks have been successfully completed and the results of the **Phase I Program** provide a firm basis for the detailed design, fabrication and test of a 94GHz "electronic" mirror capable of integration with a beam-steerable radiometric imaging system. It is planned to fully demonstrate the performance of an electronic mirror during **Phase II** through detailed test and utilization in a radiometric imaging system. A summary of the major conclusions resulting from the **Phase I Program** is given below. A detailed description is provided in **Section 3**.

- (1) Analysis of the SARI approach to all-weather imaging was performed for the three premier current and anticipated UAV platforms: the Predator, DarkStar and Global Hawk. These UAVs represent a wide range in operational altitude, ranging from 10,000 to 60,000 ft (3 to 18 km). The analysis confirmed the advantages realized through use of an electronic mirror to reduce weight, power consumption, etc. In the design study the parameters of the SARI systems were constrained by a wide array of realistic constraints, such as size, weight, number of array elements, etc. Based on this study, a passive, mm-wave, imaging system with unique surveillance capabilities and reasonable imaging characteristics is now feasible for the first time.
- (2) Significant progress in establishing feasibility for the diode array was made during Phase I. The MBE doping characteristic for the optimum monolithic diode array configuration were determined and the fabrication processes identified. The design of the required masks to fabricate the diode arrays was completed. The anti-series diode concept was investigated and the potential advantages confirmed. A system design was completed to achieve an electronic

scan capability of  $\pm 30^\circ$  at 94 GHz. Preliminary assessment of the practicality of integration of the electronic mirror into a the Predator UAV was performed.

- (3) The Phase I Report has been completed documenting the basis of the proposed innovation.

In addition to the above activities the **Phase I Program** has also revealed a growing number of application areas for millimeter-wave imaging. *IR&T* has also considered the effect of allowing active illumination during the Phase I Program. In a number of application areas this may prove a distinct advantage e.g. concealed weapon surveillance; targeting and guidance, commercial navigation/surveillance etc.

In summary, the Phase I program has been successfully completed and has served to fully establish feasibility of the proposed innovations. The quasi-optical, monolithic diode array approach to the "electronic mirror" may provide the breakthrough in cost and reliability necessary to access an all-weather, high-resolution surveillance capability. In addition, a myriad of millimeter-wave applications become possible such as weapon detection, non-destructive test, all-weather navigation, fire fighting, oil slick detection, etc. A successful demonstration of a beam-steerable radiometric imaging capability would open up a new era of all-weather surveillance.

## 2.4 References

- 2.1 M. Shoucri et al., "A *Passive Millimeter-wave Camera for Aircraft Landing in Low Visibility Conditions*", IEEE Aerospace and Electronics Systems Magazine, Vol 10 (5), May 1995, 37-42.
- L. Yujiri et al., "Passive Millimeter-wave Camera" Proceedings of SPIE Vol. 3064, SPIE Conference on Passive MMW Imaging Systems, Orlando, Florida April 21-22, 1997, 15-22
- 2.2 R-C. Chou, J.A. Lovberg and C. Martin, "More Advances in Real-time Millimeter-wave Imaging Radiometers for Avionic Synthetic Vision" Proceedings of SPIE Vol. 3088, SPIE Conference on Enhanced and Synthetic Vision, Orlando, Florida April 21-22, 1997, 2-7.
- R. Olsen, J. Lovberg et al., "Passive Millimeter-wave Imaging using a Sparse-array Antenna" Proceedings of SPIE Vol. 3064, SPIE Conference on Passive MMW Imaging Systems, Orlando, Florida April 21-22, 1997, 63-70
- 2.3 J.A. Lovberg et al., "Passive Millimeter-wave Imaging for Concealed Weapon Detection" Proceedings of SPIE Vol. 2938, SPIE Conference on Command, Control,

Communications and Intelligence Systems for Law Enforcement, Boston, Mass., Nov.21-1996, 120-30.

- 2.4 A. Pergande et al., "Concealed Weapon Detection Sensor and Signal Processing Demonstration" Proceedings of SPIE Vol. 3064, SPIE Conference on Passive MMW Imaging Systems, Orlando, Florida April 21-22, 1997, 46-53.
- 2.5 W. J. Wilson et al., "Millimeter-Wave Imaging Sensor", IEEE Trans. on Microwave Theory and Techniques **34**, 1026-1035 (1986).
- 2.6 R. Kuroda et al., "Direct-detection MMIC FPAs for MMW Imaging" Proceedings of SPIE Vol. 3064, SPIE Conference on Passive MMW Component Technology I, Orlando, Florida April 21-22, 1997, 90-97.
- 2.7 Lovberg et al., "*Advances in Real-time Millimeter-wave Imaging Radiometers for Avionic Synthetic Vision*", Proceedings of the SPIE - The International Society for Optical Engineering, Vol 2463, "Synthetic Vision for Vehicle Guidance and Control", Orlando, FL, USA, 17-18 April 1995. SPIE-Int. Soc. Opt. Eng. 1995 p. 20-7.
- 2.8 G.W. Swenson and N.C. Mathur, "*The Interferometer in Radio Astronomy*," Proc. IEEE **56**, 2114 (1968).
- 2.9 A.R Thompson, J.M. Moran and G.W. Swenson, "*Interferometry and Synthesis in Radio Astronomy*," Wiley, New York, 1986.
- 2.10 H. Suess and M. Peichl, "Airborne and Ground-based Passive Millimeter-wave Imaging at 37 and 90 GHz" Proceedings of SPIE Vol. 3064, SPIE Conference on Passive MMW Imaging Systems, Orlando, Florida April 21-22, 1997, 71-78.
- 2.11 C.S. Ruf, et al., "*Interferometric synthetic aperture radiometry for the remote sensing of the Earth*," IEEE Trans. Geosci. Remote Sensing **26**, 597 (1988).
- 2.12 C.T. Swift, et al., "*Aperture synthesis concepts in microwave remote sensing of the Earth*," IEEE Trans. MTT **39**, 1931 (1991).
- 2.13 W.W. Lam et al., "*Millimeter-wave Diode-grid Phase Shifters*" IEEE Transactions on Microwave Theory and Techniques, **36**(5) May 1988, 902-907.  
W.W. Lam et al., "Diode Grids for Electric Beam Steering and Frequency Multiplication", Int. Journal of IR & MM Waves, 27-41 (1986).
- 2.14 L. Sjogren, "Diode Array Beam Controllers", Ph.D. dissertation, E.E. Department, UCLA, 1993.  
L.B. Sjogren et al., "Phased Array Operation of a Diode Grid Impedance Surface", IEEE Trans. on Microwave Theory and Techniques, 1993.

### **3. Phase I Results**

#### **3.1 Introduction**

*IR&T* have developed designs for potential SARI systems for the Predator, DarkStar and Global Hawk UAVs. These systems demonstrate that passive radiometric imaging systems can be built with adequate performance for reconnaissance and surveillance missions, while meeting power weight and data processing limitations. The *IR&T* designs represent an order of magnitude improvement in system capability and performance as compared with previous approaches. In addition, realization of the electronic mirror, determined to be crucial for success, has been investigated via the proposed monolithic varactor diode array. The necessary molecular beam epitaxial growth profile for the GaAs wafers has been determined, mask design and fabrication procedures established, and preliminary integration into a UAV performed. The outlook for success appears excellent. The proposed **Phase II Program** will fully establish the capabilities of the electronic mirror and demonstrate electronically beam-steerable radiometric imaging. Follow-on **Phase III** funding would fully integrate a beam-steerable sparse array radiometric imaging system into the Predator (or equivalent) UAV and demonstrate surveillance performance. The **Phase II** and **Phase III** activities will continue to be carried out in close collaboration with and support from the General Atomics, a privately held company that manufactures the Predator UAV.

#### **3.2 Results**

The following Sections describe in detail the progress achieved during the current **Phase I SBIR Program**.

##### **3.2.1 Task 1 - Results**

**Objective:** Establish feasibility of sparse aperture radiometric imaging system via detailed design and analysis. The effort consisted of two broad areas:

- (1) A determination of imaging system requirements (temperature and spatial resolution, array configuration, etc), and candidate sensor platforms, generating an initial system design.
- (2) Performed a detailed system feasibility design based on the requirements identified in step 1. Design iterations lead to a final system design. Questions addressed here included:



- a. Optimization of total system size, weight, and detector number, for specified target range and required temperature and spatial resolutions.
- b. Demonstration that the point spread function (PSF) of the synthesized beam is acceptable, with sufficiently low sidelobes.
- c. Generation of feasibility designs for three candidate UAV system applications.

**Results:** The results are presented in several subsections, structured as follows: In Section 3.2.1.1 we present a potential conops for a downward-looking imaging system. In Section 3.2.1.2 the selection of potential sensor platforms is discussed, with emphasis on UAVs. Section 3.2.1.3 presents a determination of basic system requirements, such as spatial resolution, image contrast and dynamic range, imaging array configuration, how images would be built up, etc., from which an initial system configuration is presented. This is followed (Section 3.2.1.4) by an examination of the imaging performance of the proposed sparse array imaging technique, via a calculation of the point spread function (PSF) for candidate systems. The assumed weather conditions have a profound impact on system performance, as discussed in Section 3.2.1.5. Several weather models are introduced for use in system performance calculations. In Section 3.2.1.6, final system designs are presented for three different UAV platforms. In the remaining two subsections, we demonstrate that solutions are available for two other problems which previously prevented realization of practical mm-wave imaging system. First, components have been determined to be available for the mm-wave receiver and data processing system which can meet power, weight, computational load and cost constraints (Section 3.2.1.7). Second, novel solutions for the mechanical movement/vibration of the imaging array elements have been recently developed by ERIM International as part of a General Atomics research team. These are discussed in Section 3.2.1.8.

#### **3.2.1.1      *Concept of Operations (CONOPS) for a Downward Looking Imaging System***

Before addressing imaging system requirements it is essential to have in mind a specific role or conops, which the system is intended to fulfill. Defining a conops for a new imaging sensor is important given the high performance currently available from imaging SAR systems (< 1 ft resolution possible), and EO/IR imagers. *IR&T* (and others) believe that a mm-wave imaging system can provide important complementary reconnaissance and surveillance

capabilities which are otherwise unavailable, and indeed cannot be provided by side-looking SAR or EO/IR systems. Specifically, current imaging systems have the following limitations:

1. **SAR systems:** Shadowing by terrain is a serious problem in hilly/mountainous areas, and in urban/built up environments ("urban canyons"). That these shadowing effects can be an important limitation has been observed in practice in both Bosnia and Korea. In addition, there is a "nadir hole" in SAR coverage extending approximately 20-30° from nadir (i.e. maximum useful SAR depression angles are about 60-70°), due to range layover effects.
2. **EO/IR systems.** Electro-optical and/or IR imaging systems can provide very high resolution imagery and have no nadir coverage problem. However, both EO and IR systems can be defeated simply by the weather - rain, fog, clouds, and other common battlefield obscurants such as dust and smoke. Such weather conditions are prevalent, indeed standard, in many potential conflict zones.

In contrast with the above limitations on current systems, mm-wave systems are now realizable which can provide all weather surveillance capabilities and also provide imagery in valleys and urban environments. Specifically, we consider a "downward looking" mm-wave passive radiometric imaging system. Passive operation has both advantages and limitations: the chief advantage is compatibility with low-observability "stealth" platforms and missions, while the main limitation is reduced adverse weather performance as compared with a comparable system using active illumination. In this Phase I project we have concentrated on examining a passive system. In a separately DARPA funded, ARL managed program (in response to FY97 ARL BAA amendment #11), *IR&T* is participating in a General Atomics led team investigating an active mm-wave targeting and imaging sensors (the MWTIS program), including examination of an active, three dimensional (3-D) downward looking SAR system.

Thus, the conops for the imaging sensor considered here is to provide real time downward-looking imagery to the warfighter/battlefield commander at either tactical or theater level, with adverse weather/obscurant penetration capability.

### 3.2.1.2 Selection of Potential Sensor Platforms

In the current Phase I program we have concentrated on a range of UAVs as potential sensor platforms. The reasons for this choice are as follows:

1. UAVs represent a new and important US reconnaissance capability. Due to their several advantages, future plans call for a much increased emphasis on UAVs as reconnaissance and surveillance platforms.
2. *IR&T* has a close and growing working relationship with the General Atomics Company, manufacturer of the Predator UAVs currently in government service (and also of several other types of UAV). This link to General Atomics provides a route to eventual system integration and deployment which would otherwise be unavailable to a small company such as *IR&T*.
3. The altitude and speed of UAVs make them more compatible with realizing National Image Interpretability Rating Scale (NIIRS) resolution levels 4-5 (see following subsection for discussion of NIIRS) with a passive mm-wave imaging system than faster, higher performance aircraft, or satellites.
4. The low observability features of an entirely passive imaging system, as considered here, are a good match to the mission of the DarkStar, a "stealth" UAV currently under development.

**Table 1. Operational Parameters and Characteristics of Selected UAVs**

Parameter	Predator	DarkStar	Global Hawk
Altitude (feet/km)	10,000' 3 km	30,000' 9.1 km	60,000' 18.3 km
Airspeed (m/s)	36-59	>128	>177
Wingspan (m)	14.6	20	35
Fuselage length (m)	8.5	5	13.5
Available power (kW)	2 (5kW in near future)	-	-
Available payload (lbs)	450	1000	1960

In our designs, we have specifically considered the three main current and anticipated tactical/theater level UAVs:

- (a) The Predator, a Tier 2 UAV, currently in service in Bosnia
- (b) Global Hawk, a Tier 2+ UAV under development for high altitude, theater level missions
- (c) DarkStar, a Tier 3- UAV with stealth characteristics and the ability to penetrate otherwise denied airspace.

The main operational parameters which impact sensor design are shown in Table I above for the three selected UAV platforms.

#### *3.2.1.3 Determination of Basic System Requirements and Initial System Configuration*

***Spatial resolution:*** To be useful for tactical/theater reconnaissance and surveillance missions an imaging system must have both sufficient spatial resolution and image contrast to allow for target recognition. For such a mission, a National Image Interpretability Rating Scale (NIIRS) of 4 or 5 is desirable, i.e. spatial resolution of ~1-2 m, sufficient for target detection and localization, though not detailed identification of target type. Note that in all our work we have assumed a factor of two improvement in spatial resolution due to image post processing. This should be a conservative assumption, and has been built into all tables.

***Image contrast and temperature sensitivity:*** In a passive radiometric imaging system, obtaining sufficient image contrast implies having a good system temperature resolution, i.e. a good ability to distinguish small scene temperature differences. At mm-wave frequencies, this implies a system temperature resolution of a few °K [Ref. 2.5 Wilson et al.]. For comparison, in an active imaging system image contrast depends on a fundamentally different parameter, the source power - usually chosen by design so as to provide a specified image contrast level under given conditions. Details of how the image contrast are calculated are presented below in the discussion of the impact of weather models (Sect. 3.2.1.4)

***Signal dynamic range:*** Further major differences between active and passive imaging systems lie in the signal dynamic range and the detailed nature of the final image. As is well known, active

SAR systems have to cope with a very large signal dynamic range - commonly 60-70 dB. This is due to the very large difference in the power levels associated with low level backscattered radiation from a surface as opposed to high level returns from direct/specular reflections - i.e. different return mechanisms are active within a single scene. By contrast, with passive radiometric imaging only a single mechanism governs the relative pixel intensities - variations in the emissivity (reflectivity) of the materials constituting the scene. Thus, the dynamic range of the signal in a passive radiometric image is much reduced as compared with an active system, to of the order of ~20 dB. Further, active images are often difficult to interpret due to the presence of visually dominant high level direct reflections and/or coherent speckle. Both of these effects are absent in passive images, leading to a much more "visual like" final image. The visual-like properties of a mm-wave image were shown in **Fig. 2.2** earlier.

***Point spread function and integrated sidelobe levels:*** The performance of an imaging system is commonly measured via two metrics: the spatial impulse response of the system, or point spread function (PSF), and the integrated sidelobe level (ISL). The ISL measures the leakage into a single resolution cell (pixel) from all other cells in the field of view. Such leakage occurs since the system spatial response always has non-zero sidelobe levels. The integrated sidelobe level is much less important for a passive system as compared with active SAR imaging systems. The reason for this is connected to the difference in signal dynamic range as between active and passive systems. In active systems it is vital to have low integrated sidelobe levels or the image could be made worthless by prevalent "ghosts" - false signals attributed to the mainlobe location but actually generated by a strong signal source lying in a sidelobe. Consequently, a common specification for SAR systems is that the integrated sidelobe level be  $\geq 30$  dB down relative to the mainlobe. In a passive system, by contrast, there is much less signal dynamic range within the field of view. Consequently, the sidelobes will integrate to give an almost constant value for all scene pixels, i.e. "ghosts" are far less prevalent. As a result, a low ISL is far less critical for passive imaging systems, and specifications can be relaxed to ~15 dB.

***Aperture Array Configuration and Image Formation:*** In order to obtain spatial resolution in two dimensions (2-D, along and across track), a passive imaging system requires a real 2-D aperture. This is in contrast to a potential downward looking active system, if one were to be developed, which would only require a 1-D array for across track resolution, along track

resolution being provided by the synthesized antenna formed from the sensor platform motion. With passive imaging, however, SAR-like aperture synthesis techniques cannot be used as the radiation is incoherent, and a second real array is required in order to provide along-track resolution. Thus, a minimal configuration in order to provide a 2-D passive imaging capability is

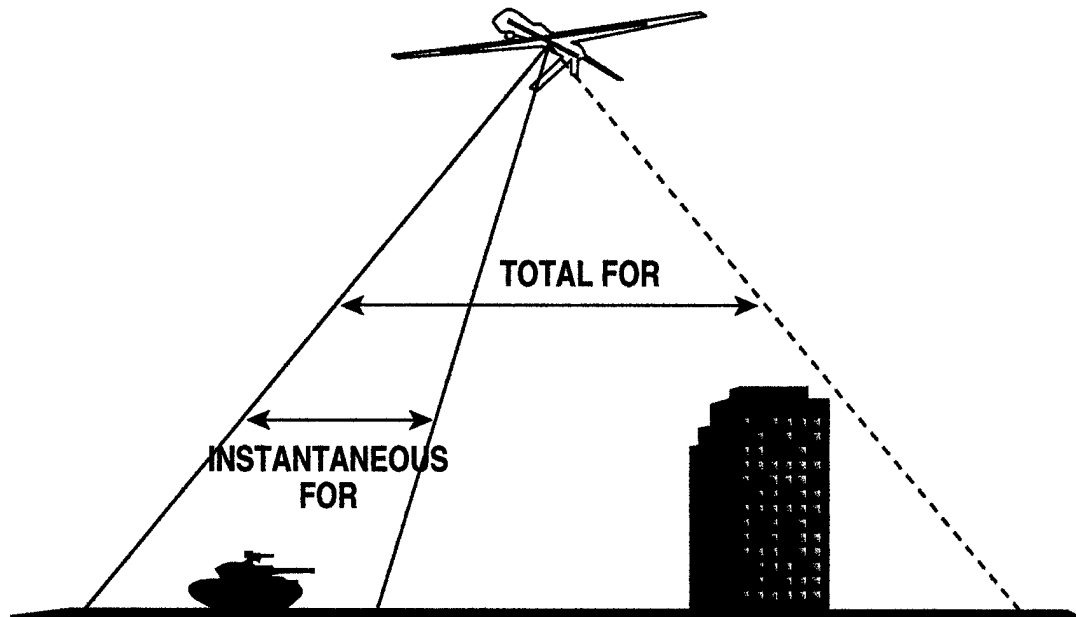


**Figure 3.1.** Schematic illustrating cross array mounted on a Predator UAV performing surveillance in an urban environment. Note that the indicated instantaneous FOR of the proposed sparse aperture system is synchronously scanned using the electronic mirrors to recover the larger system FOR.

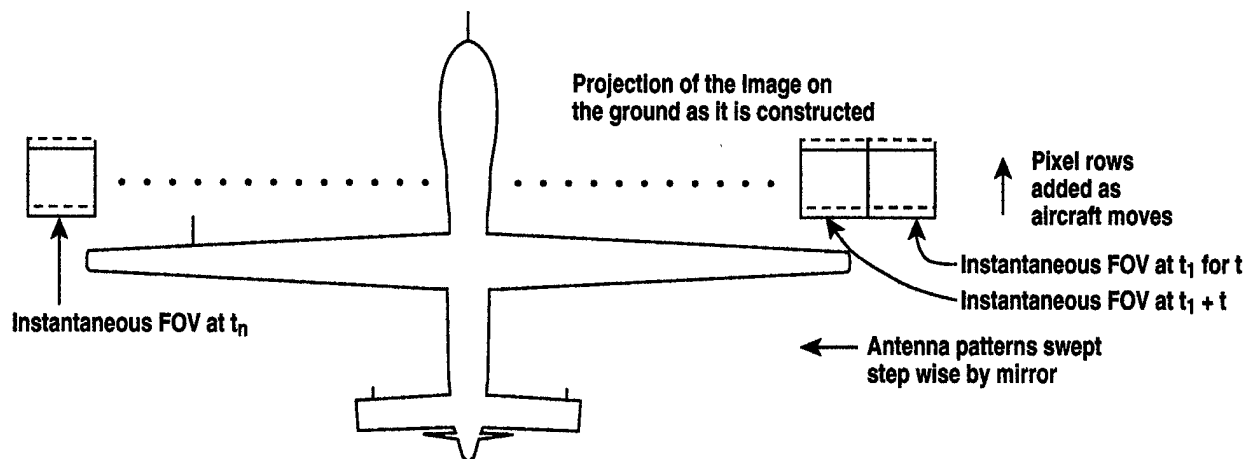


**Figure 3.2.** Schematic illustration of how the overall image from the system total FOR would be constructed as a "mosaic" by using the aircraft forward motion combined with a side-to-side scan of the instantaneous FOR implemented by the electronic mirrors.

a 2-D array in either a “cross” or a “T” configuration. **Figure 3.1** is a schematic showing such a cross array mounted on a Predator UAV, along with an illustration of how the instantaneous field of regard (FOR) of the individual receiver elements would be scanned by the electronic mirrors to achieve a larger total system FOR. The overall image from the system total FOR would be constructed as a “mosaic” by using the aircraft forward motion combined with a side-to-side scan of the instantaneous FOV implemented by the electronic mirrors. This process of image formation is illustrated in **Fig. 3.2**

**Array size (aperture diameter):** The width of the imaging array governs the spatial resolution achieved by the system, and is determined by several competing factors. First, as large an aperture as possible is desirable for maximum spatial resolution: the spatial resolution ( $\Delta x$ ) on the ground is given by  $\Delta x \approx \lambda h/D$ , where  $h$  is the height and  $D$  is the aperture width. An absolute maximum size for the aperture is set by the physical extent of the airframe, i.e. wingspan and fuselage length (see **Table I** above). Other than for the Predator and DarkStar fuselage length, however, the maximum array extent is actually set by the need to limit the number of receivers in the array. Increasing the length of an array implies more receiver elements if image quality is to be maintained (see **Section 3.2.1.4** below). We have taken ~400 receivers as a current practical limit (due to cost and computational load) on the total number of receivers employed. This implies maximum array lengths of around 13 m. As costs of MMIC components decrease, and available onboard processor power continues to increase, the practical number of receivers and hence maximum array size will increase.

**Field of Regard (FOR):** To be useful, an imaging system must be able to image a useable swath width on the ground. Clearly, the larger the FOR, the better. We have taken a FOR corresponding to a total image swath width of 2 km on the ground as a minimum acceptable performance metric. Note that in the electronically steered **IR&T** imaging concept, the total system FOR does not determine the minimum size of the individual receiver elements, i.e. in the **IR&T** approach the instantaneous field of view of the receiver elements is smaller than the total FOR, the total FOR being obtained via beam steering (this concept was described in detail in **Section 2.2.1**)

**Summary of basic system requirements:** The projected role of the mm-wave imaging system is to provide downward looking real-time imagery to NIIRS level 4-5 resolution. A summary of basic system characteristics required to meet this objective, as derived in Phase I, is shown in **Table II**. These characteristics formed the basis for an iterative design approach leading to the final system designs presented in **Section 3.2.1.6**.

Table II. Initial System Configuration and Desired Characteristics	
Parameter	Desired Metric
Array Configuration	Cross or "T"
Maximum number of receiver elements	400
Spatial resolution/PSF (m)	1-2
Temperature sensitivity, $\Delta T$ (K)	$\leq 2$
System dynamic range (dB)	20
Integrated sidelobe level, ISL (dB)	$\leq -15$
Total field of regard (deg)	$\geq 10^\circ$

#### 3.2.1.4 *Image Quality/Point Spread Function (PSF) for Candidate Systems*

As described previously, the performance of an imaging system is commonly measured via two metrics: the spatial impulse response of the system, or point spread function (PSF), and the integrated sidelobe level (ISL). Having determined that potential systems can consist of a maximum of 400 receiver elements, deployed in either a cross or T array configuration, we now need to determine if such a system will have acceptable imaging characteristics. System imaging characteristics are modeled using both one and two dimensional numerical simulation codes (Synbeam-1D and Synbeam-2D), developed by *IR&T* and implemented in the IDL programming language. Results from the codes are used as part of the iterative system design/optimization process.

The programs Synbeam-1D and Synbeam-2D calculate the synthesized antenna pattern using standard Fourier transform techniques (**Ref. 3.1**) and analytic antenna theory (**Ref. 3.2**). The antenna patterns of the individual antenna elements are first determined and the (arbitrary)

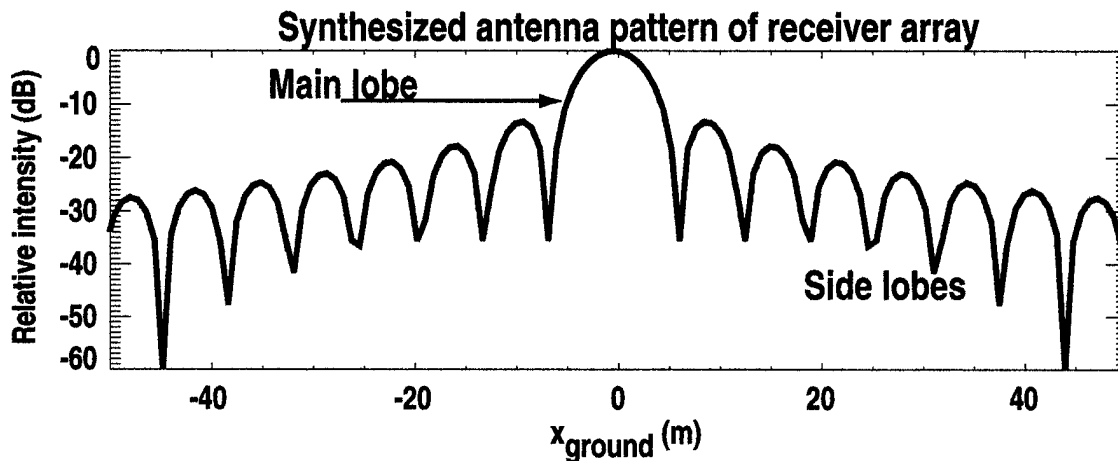


locations of all the individual receivers specified. Individual antenna radiation patterns are obtained by Fourier transforming the respective aperture distributions. The standard “array theorem” of Fourier optics is then used to obtain the total synthesized antenna pattern. This last step consists of multiplying the Fourier transforms of the individual element with the transform of the locations of the individual elements. The solution is then propagated the required distance to the ground by choosing the Fourier transform scale correctly. The codes have been checked against several known analytic solutions for specific cases and have been found to be accurate.

Examples of results and output from the 1- and 2-D versions of Synbeam follow for a potential imaging system for the DarkStar UAV, with the characteristics shown in **Table III**. Shown in **Fig. 3.3** is a 1-D plot of the central portion of the synthesized antenna pattern as a function of distance on the ground, obtained for the system specified in **Table III**. As can be seen, the pattern is regular, with a central lobe of width 3.3 m. The synthesized system antenna pattern is shown on a larger scale (corresponding to a width of 2 km on the ground) in **Fig. 3.4(a)** as a red curve. Also shown in **Fig. 3.4(a)** as a blue curve is the radiation pattern of an individual receiver antenna element (width 420 m to 3 dB points). By beam steering the individual antenna patterns, a total swath width of 3.2 km can be obtained on the ground, for the system parameters assumed (from **Table III - Section 3.2.1.6**).

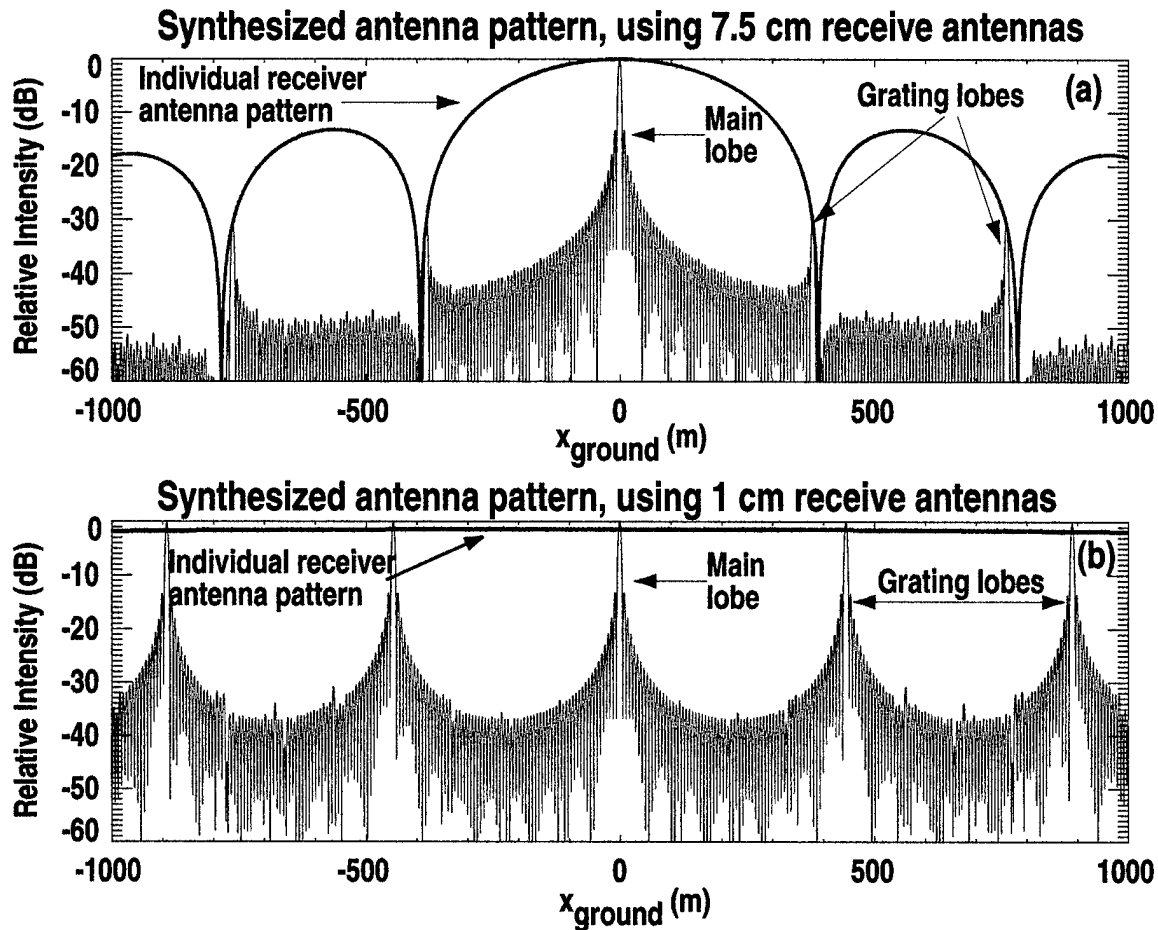
In the *IR&T* approach the finite width of the individual receiver antenna pattern plays a vital role in reducing the amplitude of the residual grating lobes visible in the synthesized pattern. The importance of this factor can be seen by comparing **Figs. 3.4(a)** and **(b)**. Figure 3.4(b) represents a conventional approach to obtaining the same swath width as the beam steered *IR&T* approach. In order to obtain a swath width of 3.2 km without beam steering, the size of the individual antenna elements must be reduced to 1x1 cm (as opposed to 7.45x7.45 cm in the *IR&T* approach), resulting in a much wider antenna pattern shown as the blue curve in **Fig. 3.4(b)**. With this much wider antenna pattern, and keeping other parameters unchanged, the grating lobes in the radiation pattern are of approximately equal amplitude to the main lobe. Such grating lobes are obviously unacceptable and make the conventional approach impractical for the system parameters chosen.

Table III. Assumed Imaging System Characteristics for Synbeam Calculations	
Parameter	Assumed Characteristics
Array Configuration	Cross with 4.5 m arms
Number of receiver elements	376
Antenna spacing	Uniform
Receive antennas	Square, 7.4x7.4 cm
Distance to target (UAV height)	30,000 ft/ 9.1 km



**Figure 3.3.** 1-D plot of central portion of synthesized antenna pattern as a function of distance on the ground, for a receiver array with the characteristics shown in Table III. The 1-D slice is taken through a principal plane.

Turning to 2-D antenna patterns, a 2-D plot showing the system point spread function is shown in **Fig. 3.5(a)** on a 0-40 dB scale. As expected from the geometry of a cross array, the highest sidelobes also have a distribution in the form of a cross. The integrated sidelobe level for this distribution is -8 dB, without any weighting/tapering of the array distribution pattern. By applying weighting functions, the desired ISL level of -15 dB can easily be achieved, though at



**Figure 3.4.** (a) 1-D plot of synthesized antenna pattern on a larger scale (red curve), for a beam steered receiver array with the characteristics shown in Table III. Shown in blue is the antenna pattern of an individual receiver. (b) 1-D plot as for (a), except that smaller, 1 cm diameter, receiver antennas are assumed, as would be required in a conventional design to achieve the same total FOR as for the beam steered design presented in (a). In this case, in order to make the individual receiver antenna pattern visible, it has been moved down on the y axis by 2 dB (i.e. actual antenna pattern is  $\sim 0$  dB in the central portion of the plot). Notice that the grating lobes are substantially reduced in (a) as compared with (b). In both plots the 1-D slices are taken through a principal plane.

the cost of some main lobe broadening. Shown in Fig. 3.5(b) is the antenna pattern of a filled rectangular aperture of diameter 4.5m, which represents the best performance that can be achieved with an aperture of this diameter. The variation between Fig. 3.5 (a) and (b) illustrate the difference in beam quality between a filled aperture (ideal case), and the sparse aperture design considered in this report. It should be noted that a filled aperture of the size considered here (4.5 m) is of course completely impractical for an airborne platform (number of receivers, cost, computational load), but the sparse aperture is realizable.

The conclusion from this modeling is that sparse apertures of the sizes and number of elements contemplated in this study are practical from the point of view of acceptable spatial resolution (PSF) and integrated sidelobe levels.

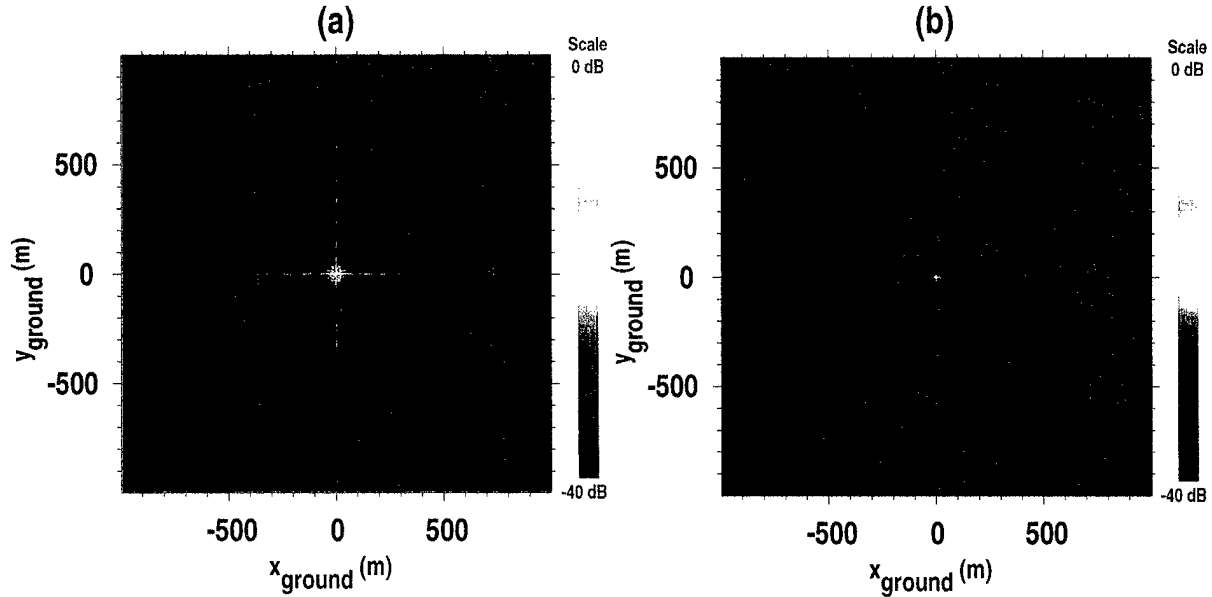


**Figure 3.5.** (a) 2-D plot of synthesized antenna pattern shown as a color contour plot (40 dB range), for a beam steered sparse aperture receiver array with the characteristics shown in Table III. The characteristic cross-shaped distribution of the sidelobes around the central lobe reflects the geometry of the cross-shaped receiver array. (b) 2-D plot for a filled aperture receiver array of the same diameter (4.5 m) as the sparse aperture considered in (a). The differences between (a) and (b) illustrate the difference in beam quality between a filled aperture (ideal case), and the sparse aperture design considered in this report.

### 3.2.1.5 Weather Model

The propagation induced attenuation at 94 GHz depends very sensitively on the weather model assumed. With progressively worse weather conditions, system performance will degrade, such that for any mm-wave imaging system weather conditions can be found for which image utility will be low. Specifically, as rain rates/cloud depths increase, absorption of the emitted radiation from the scene increases, decreasing image contrast. In the limit of very high absorption, the observed radiometric temperature of the entire scene would become uniform, with a value equal to the ambient temperature of the atmosphere. Thus, before proceeding further to design and evaluate potential imaging systems it is essential to define the weather conditions under which the systems will operate: will a proposed system produce useful images under “reasonable” weather conditions? In order to address this question in Phase I we

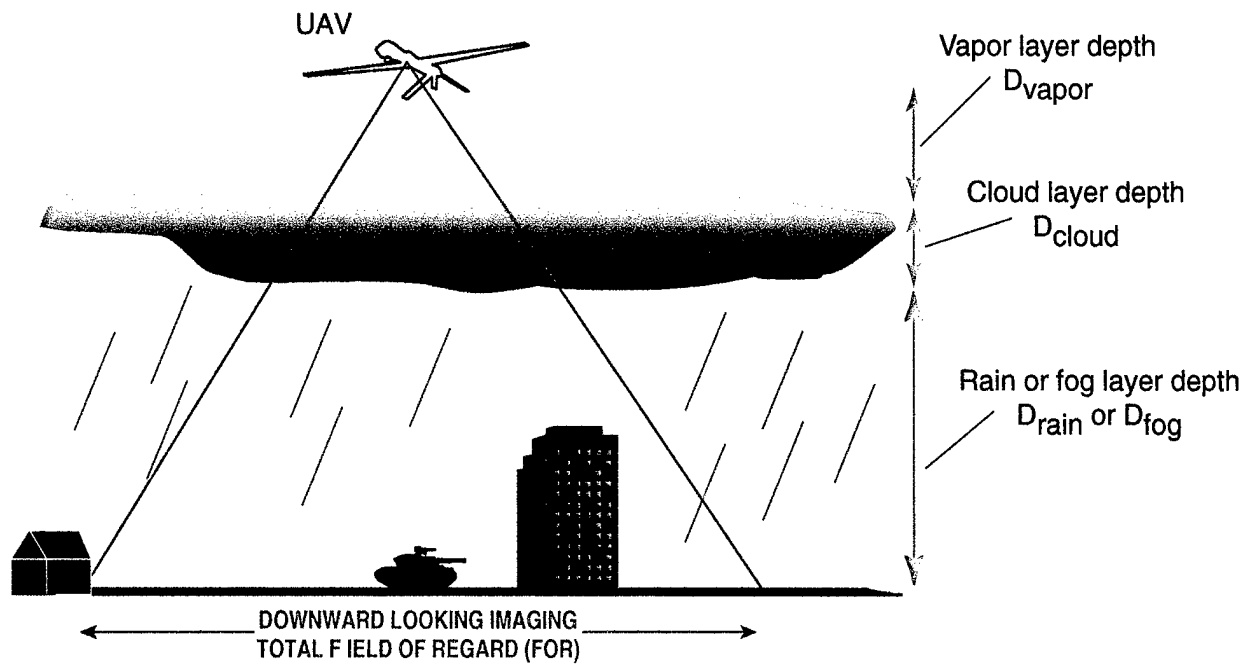
considered several weather models from clear air through to cumulus congestus cloud cover with 4 mm/hr rain. These models are summarized in **Table IV**, while **Fig. 3.6** shows schematically how the various weather layers are distributed in the models.

Table IV Weather models used in system design calculations					
Weather model	Depth of various layers (km)*				Sky temperature $T_{sky}$ (K) at 94GHz
	$D_{rain}$	$D_{cloud}$	$D_{fog}$	$D_{vapor}$ (depends on UAV altitude)	
Clear air: clear sky, light water vapor	0	0	0	“	60
Clear sky, light fog/light smoke	0	0	1.0	“	60
Moderate to heavy fog or clouds, no rain	0	1.0	0	“	120
4mm/hr rain low lying stratus	0.5	0.5	0	“	180
4mm/hr rain cumulous congestus	1.6	0.4	0	“	180

Loss values used in calculations are: 4mm/hr rain: 4.43 dB/km; cloud 0.875 dB/km; fog 0.6 dB/km; vapor 0.16 dB/km.

The more severe weather models adopted (low lying stratus and cumulus congestus) are standard models from **Ref. 3.3**. It should be noted that the 4 mm/hr rainfall rate assumed in these models has been used as a benchmark in other government programs (e.g. MWTIS program in response to ARL FY97 BAA amendment #11). In addition, all the inclement models (i.e. all models other than the clear air scenario) contain conditions under which IR/EO sensors would be defeated.

The impact of the weather on the scene temperature contrast is calculated in standard fashion, following **Ref. 2.5**. The components of the scene contributing to the observed radiometric temperature as viewed from above are illustrated in **Fig. 3.7**.



**Figure 3.6.** Schematic illustration of how various weather layers are distributed in the weather attenuation models used in this report.

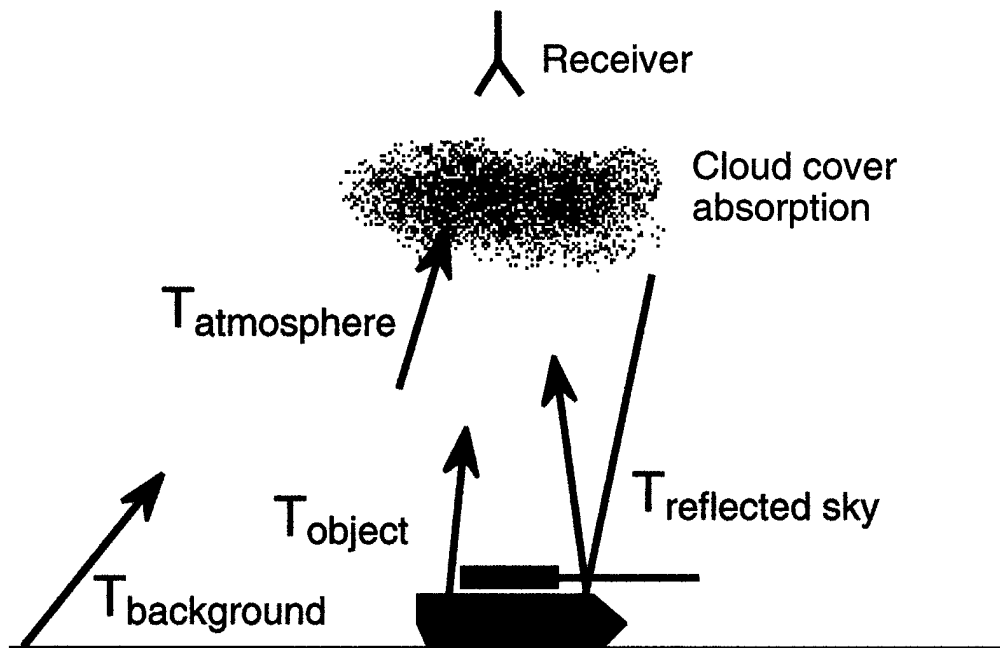


**Figure 3.7.** Components of the scene contributing to the observed radiometric temperature when viewed from above

The radiometric temperature observed ( $T_{\text{rec}}$ ) by an airborne system from a target object is affected by several factors:

$$T_{\text{rec}} = T_{\text{object}} + T_{\text{reflected sky}} + T_{\text{atmos}} \text{ (K)},$$

where we have assumed that the object fills the antenna beam. The apparent object temperature is determined by the object's physical temperature  $T$ , its emissivity  $\epsilon$ , and the atmospheric attenuation ( $L_a$ ).

$$T_{\text{object}} = \frac{\epsilon T}{L_a}.$$

The reflected sky emission from the object is given by,

$$T_{\text{reflectedsky}} = \frac{(1 - \epsilon)T_{\text{sky}}}{L_a},$$

where the apparent sky temperature is given by

$$T_{\text{sky}} \cong T_{\text{atm}} \left(1 - \frac{1}{L_z}\right) + \frac{T_{\text{cb}}}{L_z},$$

and  $L_z$  is the total zenith absorption factor,  $T_{\text{atm}}$  is the mean atmospheric temperature and  $T_{\text{cb}}$  is the cosmic background temperature. Finally, the atmospheric emission below the radiometer is given by

$$T_{\text{atmos}} = T_a \left(1 - \frac{1}{L_a}\right),$$

where  $T_a$  is the physical temperature of the atmosphere below the radiometer. As can be seen from the above formulae, the weather directly affects several components of the measured temperature.

The "signal" obtained by a radiometer is the temperature difference (contrast) between the  $T_{\text{rec}}$  observed for the target of interest and the temperature observed for the surrounding background,

$$\Delta T_{\text{sig}} = T_{\text{rec}} (\text{target}) - T_{\text{rec}} (\text{background}).$$

As with SAR systems, we can now define a point-target-contrast-ratio (PTCR), which measures the observability of a point target in clutter,

$$\text{PTCR} = \Delta T_{\text{sig}} / \Delta T,$$

where  $\Delta T$  is the system temperature sensitivity. In this report the PTCR is used as the standard measure of system performance with regard to image contrast, and is calculated for a metal target in a background consisting of earth or vegetation.

As an example of the impact of the assumed weather conditions on imaging system performance at 94 GHz, we show in **Table V** a comparison of the performance of a single point system design (that appropriate for the Darkstar UAV, see Sect 3.2.1.6, below) under different weather conditions. In this example the airborne platform is at an altitude of 9.1 km (30,000 ft). The major parameter to focus on is the variation in the obtainable Point Target Contrast Ratio (PTCR) for the various weather scenarios, assuming a metallic target.

<b>Table V. Received temperatures (K) and PTCR for various weather models and metallic target (UAV altitude 9100m).</b>				
Weather model	$T_{\text{target}}$	$T_{\text{background}}$	$\Delta T_{\text{sig}}$	PTCR
Clear air; 9.1 km light water vapor	174.9	281.8	106.9	82
Clear sky; 1 km light fog/smoke	186.0	282.6	96.6	74
1 km of moderate to heavy fog or clouds	217.8	284.8	67.0	52
4mm/hr rain, low lying stratus	255.5	287.5	32.1	25
4mm/hr rain cumulous congestus	274.9	288.9	14.0	11

Several conclusions can be drawn from the **Table V**: The point design assumed for this calculation results in acceptable target contrast ratio under all conditions. The calculated contrast ratios vary from excellent under clear air conditions (PTCR of 82) to reasonable in the cumulous congestus inclement weather model (PTCR of 11). More severe weather conditions would of course further reduce the PTCR.

#### 3.2.1.6 *Final System Designs*

Arriving at a final design was an iterative process, involving the use of the design formulae for the beam steered *IR&T* approach presented in **Section 2.2.1**, and also all the factors considered in the preceding sub-sections, i.e. imaging requirements in order to meet the projected conops, practical limitations on the number of receiver elements, etc. From this



process we have developed possible SARI designs for the Predator, DarkStar and Global Hawk UAVs, as shown below in **Table VI**, using the median case (moderate to heavy fog or clouds) weather model for performance calculations.

<b>Table VI. Millimeter SARI Design Parameters for Selected UAVs</b>			
Parameter	Predator	DarkStar	Global Hawk
UAV altitude (feet/km)	10,000' 3km	30,000' 9.1km	60,000' 18.3km
Airspeed (m/s)	35	>128	>177
Ground spatial resolution (m)*	0.7	3.3	2.2
Field of regard (degrees)	$\pm 20^\circ$	$\pm 10^\circ$	$\pm 5^\circ$
Imaged swath width on ground (meters)	2200	3200	3200
Number of detectors	400	400	400
Individual antenna diameter (cm)	6	6	6
Synthesized array diameter (m)	7	4.5	13
System temperature sensitivity $\Delta T$ °K	4.1	1.3	6.4
PTCR	16	52	7
System power draw (kW)	0.6	0.6	0.6
Total system weight (lbs)	175	175	175
Available payload (lbs)	450	1000	1960

As can be seen from the **Table VI**, performance varies for each UAV. All systems closely approach or meet desired metrics: all the systems have an image swath width of over 2 km, with spatial resolution varying from 0.7 to 3 m. It is important to realize that the spatial resolution can of course be improved simply by flying lower, i.e. at an altitude of 15,000 ft the

DarkStar system would have a spatial resolution of 1.6 m. The point-target-contrast-ratios (PTCR) obtained using the median case weather model vary from good for the Predator and Global Hawk (PTCRs of 7 and 13), to excellent for the DarkStar (PTCR of 52). The PTCRs in the table are calculated for the maximum spatial resolution, better PTCRs can be obtained for larger scale structures by adaptive data processing, i.e. the achieved contrast ratios are scale dependent.

<b>Table VII. Comparison of point-target-contrast-ratios (PTCR) and received temperature differences (<math>\Delta T_{sig}</math>) for different UAV platforms and weather models</b>						
Weather model	UAVs					
	Predator		DarkStar		Global Hawk	
	$\Delta T_{sig}$	PTCR	$\Delta T_{sig}$	PTCR	$\Delta T_{sig}$	PTCR
Clear Sky, light water vapor	133.9	25	106.9	82	76.2	12
Clear sky/light smoke, 1km light fog	121.0	23	96.6	74	68.8	11
Moderate to heavy fog or clouds, 1 km thick	83.9	16	67.0	52	47.8	7
Low lying stratus, 4mm/hr rain	40.1	8	32.1	25	22.8	4
Cumuluous congestus, 4mm/hr rain	17.5	3	14.0	11	10.	2
UAV altitude	3.0 km		9.1 km		18.3 km	

How the performance of the SARI systems on the different UAV platforms would vary with weather conditions is shown in **Table VII**. Under clear conditions, as expected, all systems perform well, the DarkStar in particular, while adverse weather performance is acceptable. Improved adverse weather performance can be obtained by using active illumination, but at the cost of the stealth advantages of a purely passive system.

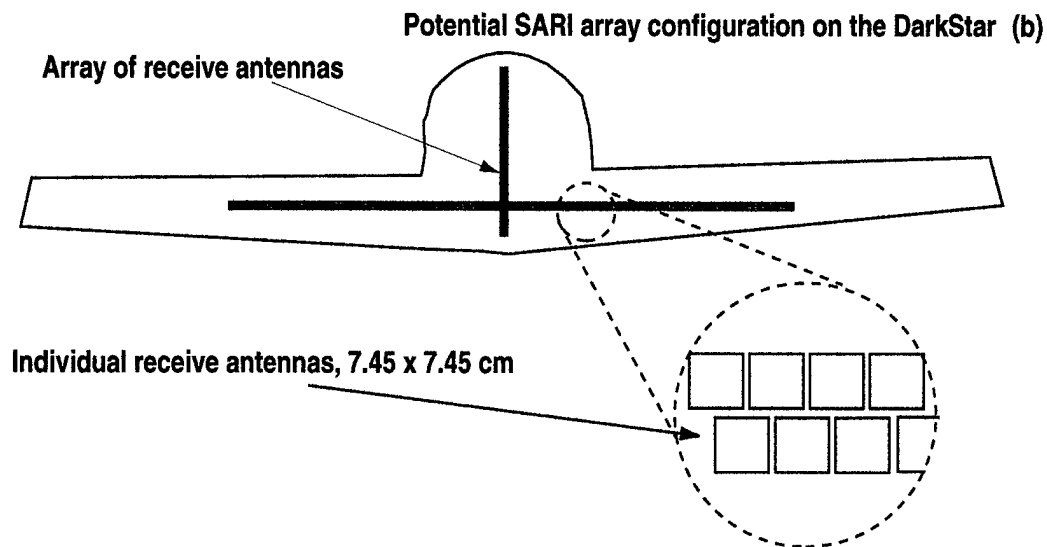
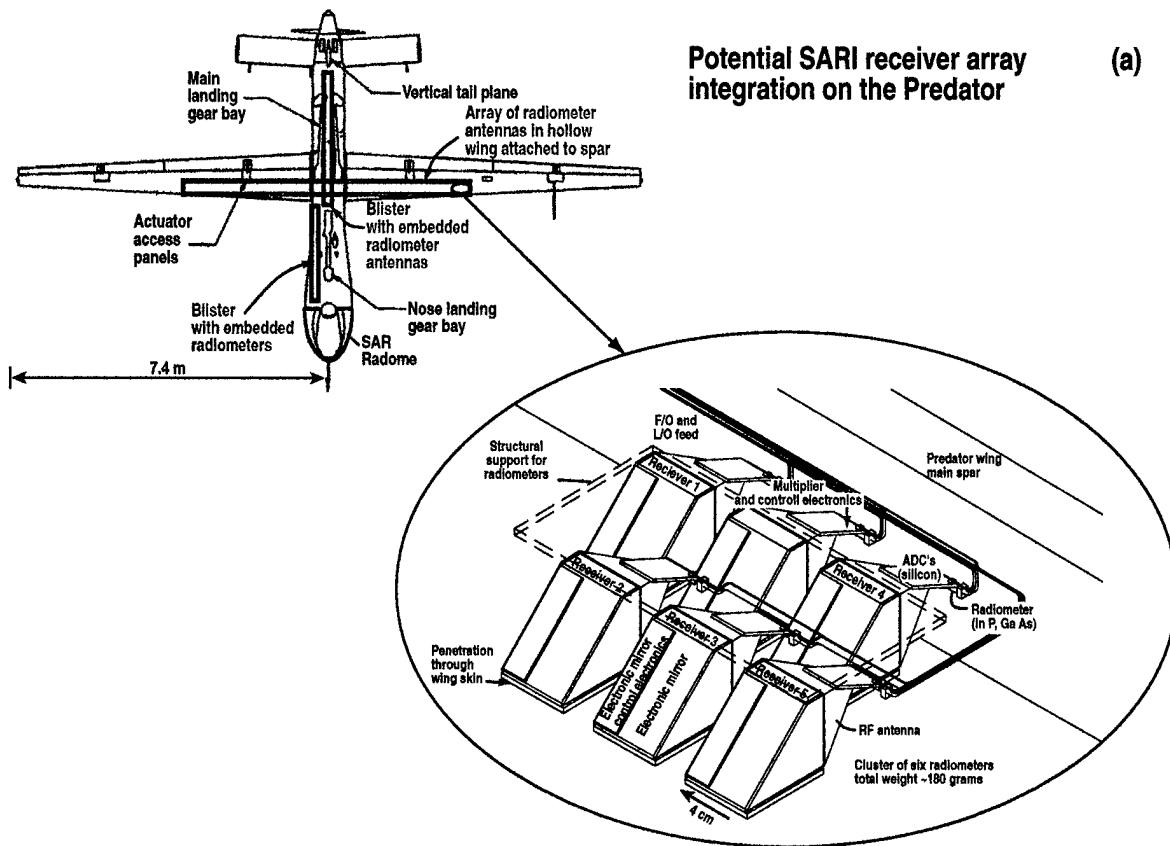


**Figure 3.8.** (a) Illustration of a SARI system using a cross array configuration integrated into the Predator UAV, with enlarged detail of a cluster of six receiver elements attached to the main wing spar structure. (b) Cartoon showing potential “T” imaging array configuration on a DarkStar UAV.

With the assistance of General Atomics we have investigated the practicality of mounting a SARI system with the characteristics shown in **Table VI** on the Predator UAV. **Figure 3.8a** shows an outline drawing of a SARI system with a cross array configuration integrated into the predator with a larger detail showing a cluster of 6 receiver antennas in the wing. The SARI system will fit in the Predator while meeting all power, weight and volume constraints. Shown in **Fig. 3.8(b)** is a cartoon showing how a 9x4.5 m array in a “T” configuration could fit on the DarkStar.

The total system weight and power draw for a 400 receiver element system was estimated using numbers for MIMIC circuitry, local oscillator and processor power draw, along with weight estimates for antennas and antenna mounting structures, etc. Again, projected performance meet the constraints imposed by the potential UAV platforms. **Figure 3.9** shows

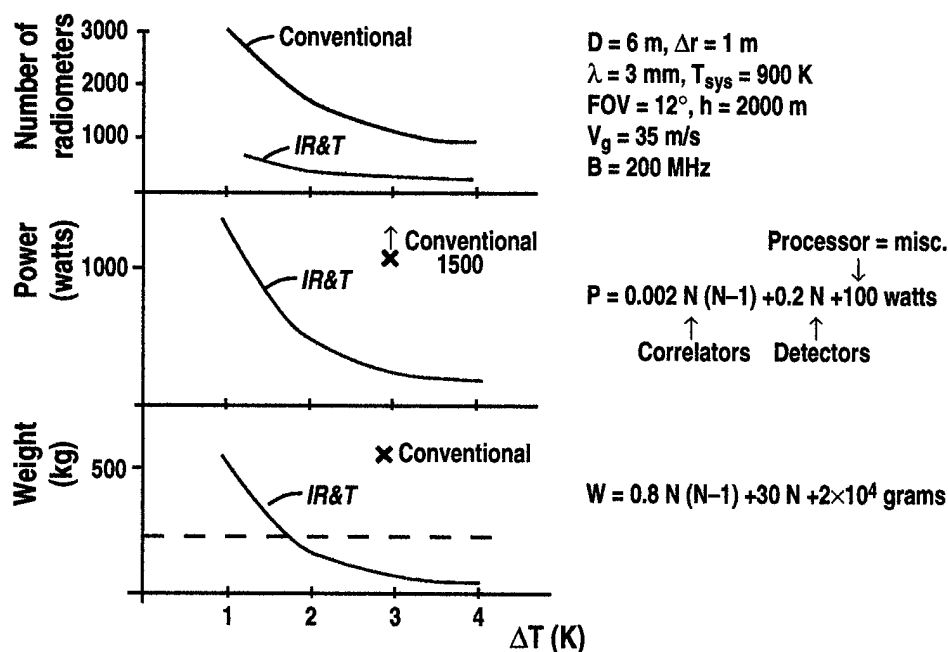


**Figure 3.9.** Showing the number of receivers, system power draw and weight, as a function of system performance, as represented by the system temperature sensitivity ( $\Delta T$ ), for both the beam steered **IR&T** design approach, and a conventional, non-beam steered design. The design parameters for the comparison, and the estimates used for the system power and weight, are shown in the figure. In all cases, the **IR&T** design provides much improved performance as compared with the conventional design.

the number of receivers, system weight and power draw, as a function of system performance, as represented by the system temperature sensitivity ( $\Delta T$ ), for both the beam steered **IR&T** design

approach, and a conventional, non-beam steered design. The design parameters for the comparison, and the estimates used for the system power and weight, are shown in the figure. As can be seen, the *IR&T* design provides dramatically improved performance as compared with the conventional approach.

In conclusion, *IR&T* have developed designs for potential SARI systems for the Predator, DarkStar and Global Hawk UAVs. These systems demonstrate that passive radiometric imaging systems can be built with adequate performance for reconnaissance and surveillance missions, while meeting power weight and data processing (see following sub-section) limitations. The *IR&T* designs represent an order of magnitude improvement in system capability and performance as compared with previous approaches.

#### *3.2.1.7 Data Processing and mm-wave Receiver Requirement*

Achieving practical onboard data and image processing for a downward-looking mm-wave imaging system is challenging, requiring low power, high throughput processing. Until recently, the required performance was unavailable, but continuing technical advances in many areas now combine to make such processing feasible using COTS hardware. For an interferometric imaging system a significant difference compared with current SAR radar image processing, which tend to use general purpose (GP) processors, is that the dedicated computations required in order to perform the data cross-correlations can be performed in hardware. This significantly contributes to achieving a practical system.

The total amount of data generated by the 150–400 detectors anticipated in the baseline system is about  $10^{11}$  samples/s for a 200 MHz bandwidth receiver system. A sparse array inversion requires of the order  $n^2$  correlations ( $n$  = number of detectors) at the bandwidth of the system. This corresponds to roughly  $10^{13}$  correlations/s for a 200 MHz bandwidth, 400 detector design. Performing the necessary computations for calibration, motion compensation in real time, etc., requires an aggressive approach to implementing the computational engine. The required performance can be achieved within the available power, weight, and volume requirements by the application of advanced distributed computing techniques, techniques that have only recently become available in the speeds and densities required.

The computation engine can be divided into two types of processing elements: hardware-based elements that directly implement selected algorithms in hardware using parallel distributed arithmetic techniques, and conventional DSP processors arrays implementing the remaining algorithms in software. A candidate architecture for the computational engine is shown in Fig. 3.10. In the following subsections we discuss the requirements of each of the subsections shown in Fig. 3.10, and candidate technology available to implement them.

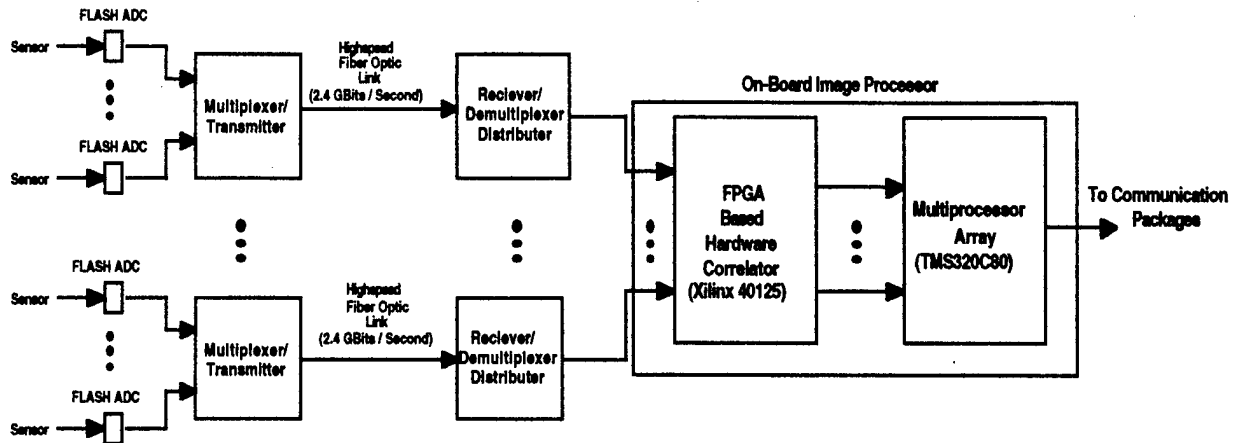


**Figure 3.10.** Data stream path and processor architecture for the SARI system

**Processing Elements:** In Table VIII estimates of the processor requirements for the software tasks needed for a passive system are tabulated along with a possible processor type, number of processors required, and the power consumption. A preliminary conclusion is that all of the processing can be done on UAV platforms. If all of the processing can be done onboard as we expect, the downlink bandwidth required is only ~4.5 Mbps for the baseline system.

Software Task	No. Calculations/s	Processor Type (No.)	Power (Watts)
3 bit correlations	$10^{13}$	FPGA XC40125s (10)	60
Image inversion	$4 \times 10^7$	DSP (TMS320C80) (0.1)	0.05
Motion compensation	$10^8$	DSP (TMS320C80) (0.21)	0.1
Image enhancement	$2 \times 10^9$	DPS (TMS320C80) (2)	10

**Analog to Digital Converters.:** Achieving the high sample rate of 400 MSPS requires a correspondingly fast analog to digital converter with a resolution of 3 bits. An optimal approach would be to integrate the ADCs into the receiver units to reduce phase errors from analog data lines. COTS Flash ADCs have the speed and resolution required but the power required is higher than is desirable (~1 Watt/ADC) and custom devices may be needed.

**Fiber Optic Transmitter and Receiver Link:** A fiber optic transmitter/multiplexer and the corresponding receiver/demultiplexer could be implemented with MMIC based custom ICs to reduce power and size. For the fiber optic channel (both transmitter and receiver), high speed (2.4 GHz) FDDI technology could be used.

**FPGA Based Correlators:** In order to meet the required processor throughput key algorithms will be implemented in hardware. Specifically, the high speed correlation could be done with Xilinx XC40125 or later FPGAs. Implementing the algorithm in hardware and using parallel distributed arithmetic (PDA) techniques yields an improvement in processing of at least 17 times the throughput available with conventional digital signal processors. A total of about  $3 \times 10^5$  correlators are required. Using the XC 40125 we estimate that 16,000 correlations and needed interconnections can be made per device. This corresponds to about 0.1 g/correlation and 0.2 mW/correlation (60 Watts total)

**Digital Signal Processor Array:** The processor array will be composed of TMS320C80 or later devices. These chips are comprised of four advanced computational units and a RISC master processor integrated on a single chip. Each TMS320C80 delivers approximately two billion RISC-like operations per second (2 BOPS). These processors are specifically designed to operate in a multiprocessor environment and have built in inter-processor communications facilities.

**MMIC Receiver:** The sensitivity of the overall imaging system is strongly dependent on the noise of the first mm-wave component in the radiometer. We have considered several options for the receiver construction, including discrete components and MMIC technology. Options for the first mm-wave component included low noise 94 GHz amplifiers (LNA) and low noise mixers. Due to power, weight and size considerations it is clear that MMIC construction is the only viable option. MMIC LNAs are the obvious choice for the front end of the radiometer due to advances in MMIC LNA technology such as the Hughes InP HEMT MMIC LNA. These

devices have been demonstrated with a noise figure of 4 dB with 22 dB gain at 94 GHz. This translates into a system noise temperature of about 750 K for the system concept described.

#### 3.2.1.8 *Motion Compensation*

In order to obtain accurate imagery from a mm-wave receiver array we need to know the relative positions of all the array elements to within a fraction of a wavelength. On a UAV platform, the wings will flex, there are pitch and roll motions, and vibration is present, so it is vital to have an accurate method to measure and compensate for the relative motion of the array elements. Unlike SAR, systems, where the dominant phase error is induced by radial motions of the platform, a downward-looking imaging sensor is relatively insensitive to radial motion, and the dominant phase error will be that induced by wing flexure. For example, the tips of the Predator wings can have motions up to 18 inches, which will result in phase errors of many wavelengths (as much as 140). Two approaches have been developed to deal with this problem, as discussed below.

Our first motion compensation concept employs a layered approach. The first layer is to use strain gauges imbedded within the aircraft structure to measure the real time flexure of the wing and fuselage. These measurements, together with a validated, existing mechanical model of the wing shape as it flexes, will provide an estimate of the phase error. We expect the residual relative phase error from the mechanical measurement to be less than  $2\pi$  (one wavelength). Two other motions that could cause large phase errors are changes in roll and pitch of the platform. Measurement by a pair of existing INSs on either side of the fuselage and another pair fore and aft would provide the additional information to correct most of these errors. A second layer is to reduce the total number of elements whose motion must be tracked, by mounting the receiver element in clusters. Each cluster of about six receivers, is mounted to a rigid, unloaded structure so that the cluster elements move together (see Fig. 3.8 above). Also, each cluster can have some vibration isolation built into the rigid mount.

The next order of improvement in phase correction will come from the phase closure approach commonly used in radio interferometry. It exploits the fact that there are  $N-1$  different phase-error terms, but after correlating each of  $N$  elements with  $(N-1)$  other elements, there are  $N(N-1)/2$  measured correlation values, giving redundant measurements of the phase errors.



ERIM (with which *IR&T* has a link through the separate DARPA funded MWTIS program) has demonstrated phase closure correction using a least squares method. Any remaining phase errors can be corrected with phase retrieval algorithms that use a priori constraints about the scene. A priori information includes such things as image non-negativity and the fact that maximizing image sharpness using one of the Muller-Buffington metrics points minimizes phase errors. Sharpness maximization requires only image structure, not prominent points. These algorithms will correct all sources of phase errors, besides the wing flexure and roll and pitch described above, including vibration, unknown internal path delays, the phase stability of the IF local oscillator, etc.

A second, novel approach to vibration/motion compensation has been developed by ERIM as part of the GA-led team working on the development of the DARPA funded/ARL managed MWTIS program (Millimeter Wave Targeting and Imaging Sensor program) which is investigating *active* mm-wave imaging systems. This approach involves the use of low power active transmitters in a proprietary approach. Using transmitters would of course imply that the system is no longer entirely passive. However, the sources would be very low power (as the beams simply reflect from the entire scene - the active beams are not being used to spatially resolve the ground), and could be frequency agile, such that the likelihood of detection is minimal.

### 3.2.2 Task 2: Results

**Objective:** Establish feasibility of the proposed “electronic mirror” concept based on an electronically controlled surface impedance consisting of an array of monolithically fabricated varactor diodes. Perform preliminary design of a practical varactor diode array for  $\pm 30^\circ$  beam-steering

#### **Results**

##### **(a) Basic Design Principles**

As described earlier in Section 2 realization of the electronic mirror concept is based on the development of a large aperture monolithic diode array. A research group at Caltech led by **Prof. D.B. Rutledge** first realized the potential for monolithic diode arrays to be utilized for electronic beam-steering. **Lam (Ref. 2.13)** proposed that beam-steering could be achieved through a simple extension of a frequency selective surface (FSS) based on a series-resonant or self-resonant grid. A series-resonant FSS consists of an array of metallic strips deposited on a semiconductor substrate interrupted by gaps at periodic intervals (see **Fig. 3.11a**). To an incoming electromagnetic wave such an FSS appears as an inductance (resulting from the metallic strips) in series with a capacitance (resulting from the periodic gaps). Such a FSS can be modeled, in a simplified form, as a transmission line with a series LC circuit as illustrated in **Fig. 3.11b**. **Kim et al (Ref. 3.4)** have shown that variation of the gap capacitance simply through dimensional changes can result in *fixed angle* beam-steering as shown in **Fig. 3.12**. As illustrated in **Fig. 3.11c**, if the gap capacitances are replaced with varactor diodes together with orthogonal bias lines, the spatial variation of the surface capacitance can then be controlled electronically.

Such an active FSS including the varactor diodes can also be modeled as a transmission line as illustrated in **Fig. 3.13** where the array appears as a shunt impedance across transmission lines with characteristic impedance  $Z_0 = \eta = \sqrt{\mu/\epsilon}$ . In this model the horizontal bias strips (see **Fig. 3.11c**) are described by  $C_{\text{bias}}$ . Typically the capacitance for this component is very small and so it has negligible effect on the array behavior at the operating frequency.  $C_{\text{diode}}$  and  $R_{\text{diode}}$  represent the variable capacitance and series resistance of the varactor diode. The gaps in the

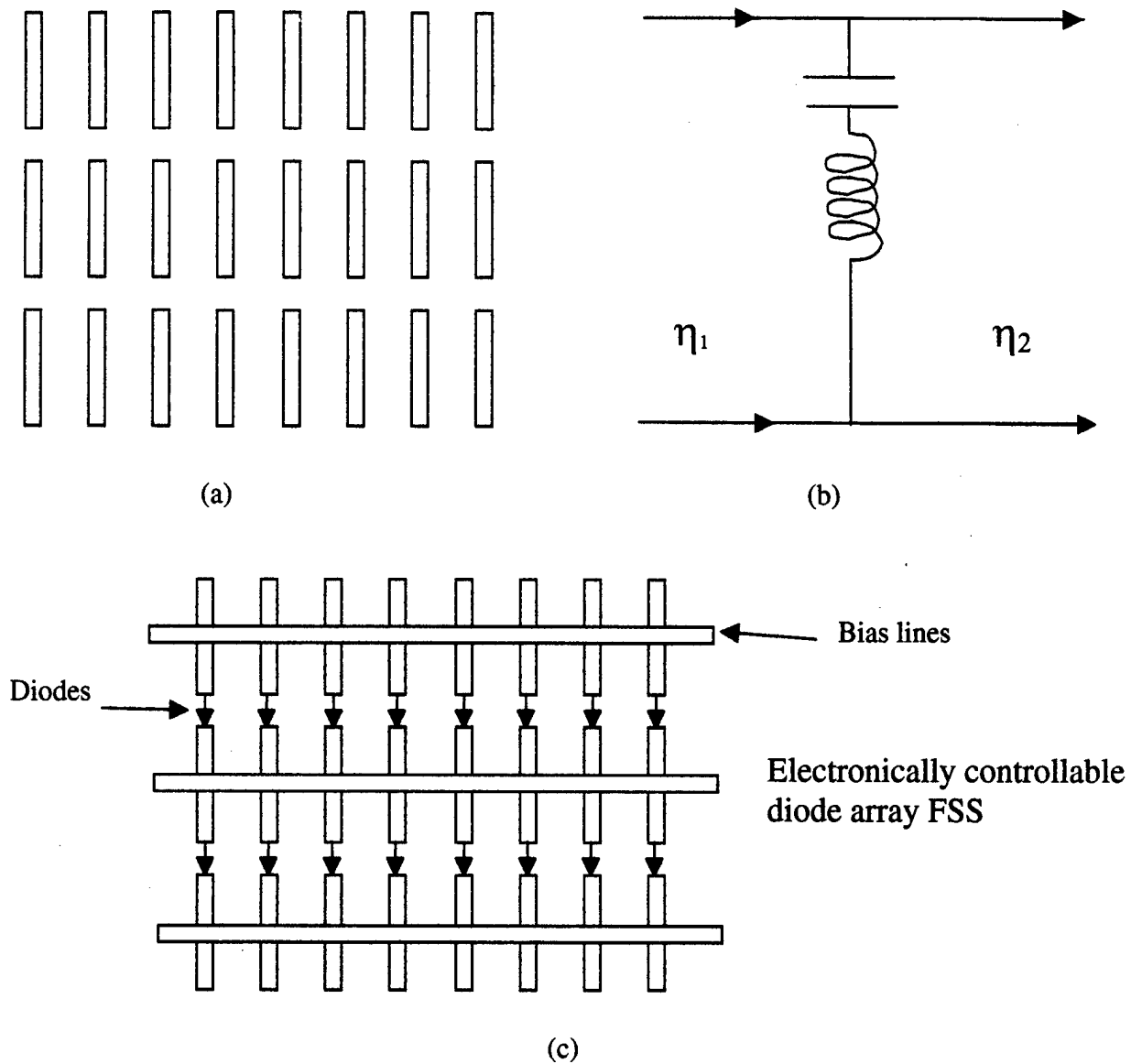


**Figure 3.11** (a) Series-resonant frequency selective surface (b) Transmission line model of series-resonant grid (c) Active version of series-resonant grid where electronically biasable varactor diodes are inserted into the capacitive gaps.

grid array also create a so-called grid capacitance that is in parallel with a fixed parasitic capacitance related to the detailed geometry of the metallization in the region of the diode. These two capacitances are in parallel and are represented by  $C_{\text{parasitic}}$  in Fig. 3.13.

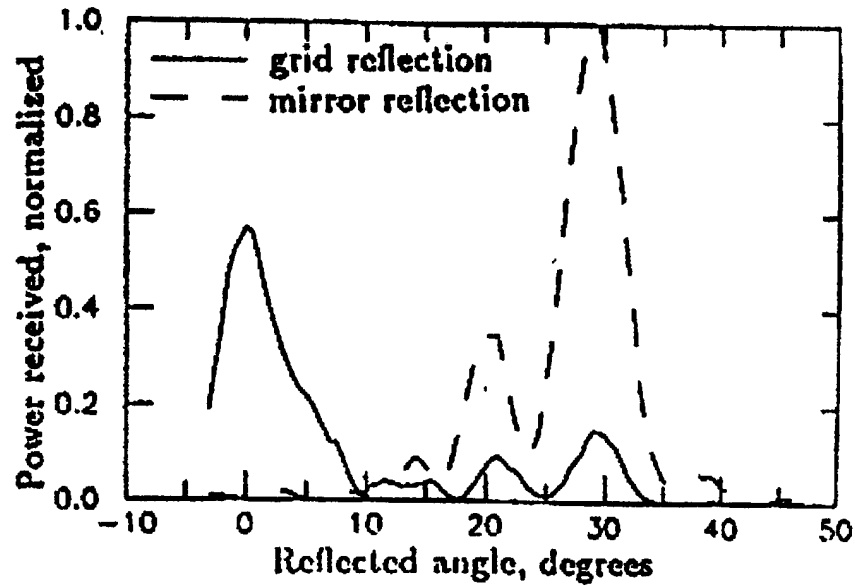


**Figure 3.12 .** Fixed angle beam-steering produced by varying the gap capacitance across a silicon wafer. The gap capacitance is varied by dimensional changes in the metallization across the wafer. (After Kim et al. Ref. 3.4)

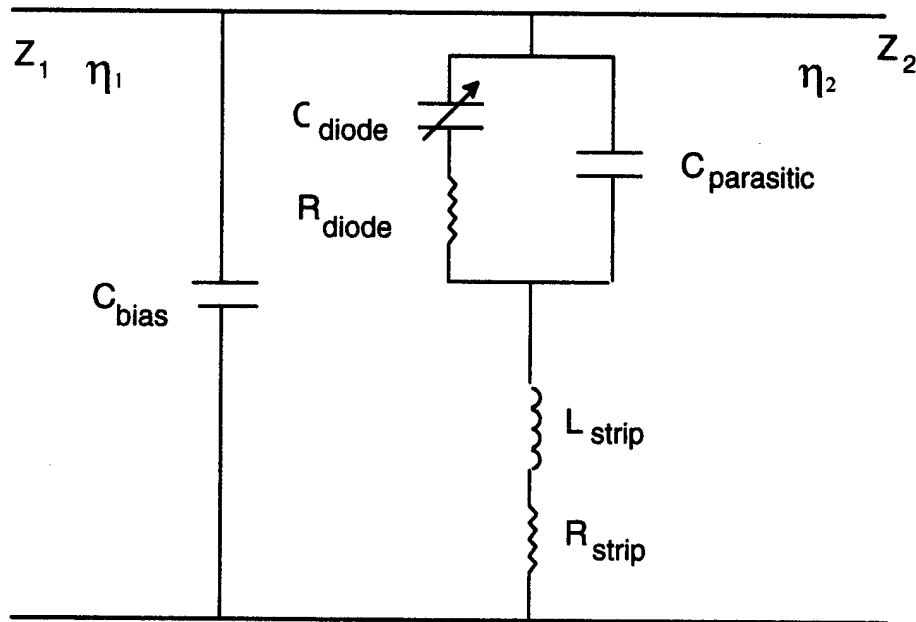


**Figure 3.13** Transmission line model for an active FSS where  $C_{diode}$  is controllable electronically.

**IR&T** have calculated, using a quasi-static model (Ref. 3.5), the grid inductance and bias

line capacitance at 94GHz. The results are illustrated in Figs. 3.14, 3.15 and 3.16 and can be easily scaled to other frequencies by scaling all dimensions, inductances and capacitances by  $f^{-1}$ .

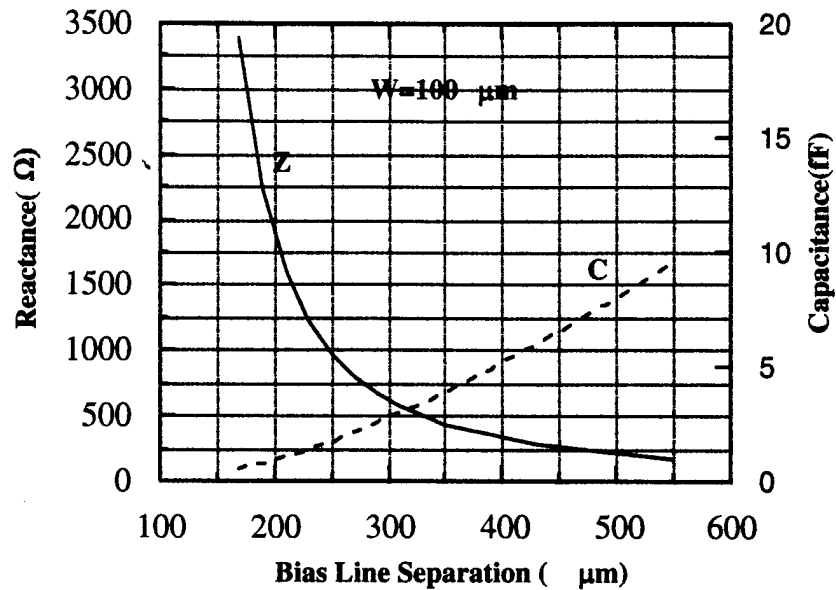


**Figure 3.14** Calculated capacitance and reactance for a bias line with width 100  $\mu\text{m}$

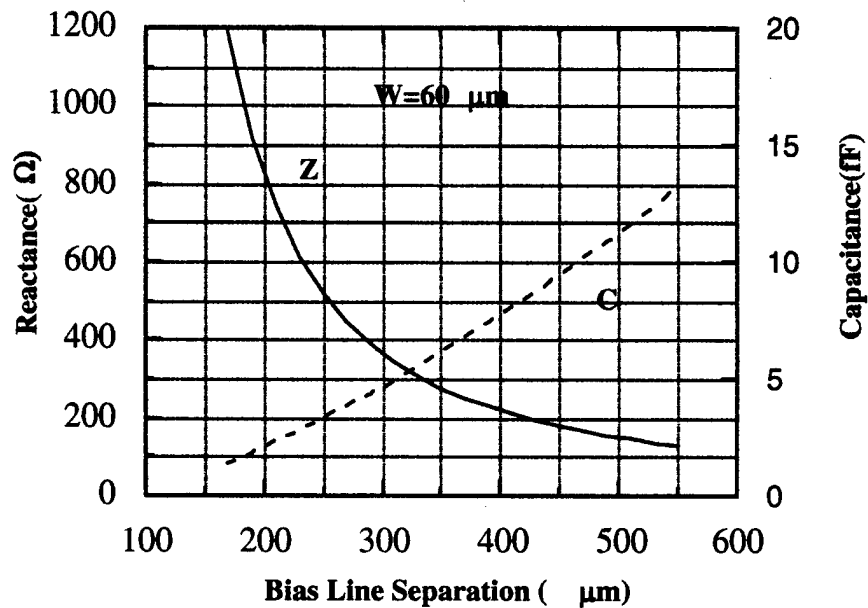


**Figure 3.15** Calculated capacitance and reactance for a bias line with width 60  $\mu\text{m}$

*IR&T* has considered the effect of the metallic bias capacitance on the achievable phase range for the beam steering arrays. In order to reduce the bias *resistance* and capacitance, the

bias line should be kept as wide as possible. Figures 3.14 and 3.15 show the computer simulated capacitance due to a horizontal bias line with widths of 60 and 100  $\mu\text{m}$ . As can be seen, with a line width of 100  $\mu\text{m}$  and a bias line separation of 300  $\mu\text{m}$ , the bias capacitance is less than 3 fF. The capacitive reactance is therefore almost in the  $\text{k}\Omega$  range, and so the *bias line alone acts in a manner similar to an open circuit at the operating frequency*. The reactance was calculated at a frequency of 94 GHz. Therefore, if we choose a bias line width greater than 100  $\mu\text{m}$ , the associated capacitance will have very little effect on the array phase control circuitry.

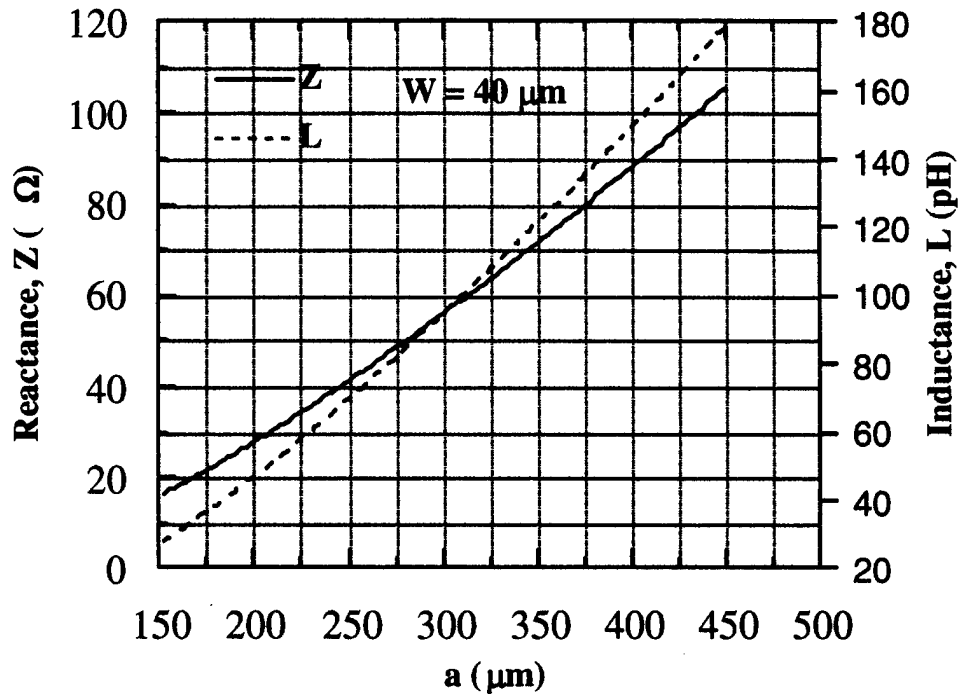


**Figure 3.16.** Calculated inductance and reactance versus strip separation for a diode antenna with width 40  $\mu\text{m}$

In order to produce large (e.g.  $\pm 30^\circ$ ) beam-steering the phase variation (or impedance variation) has to be maximized across the array. As mentioned above, the diode array is equivalent to a series RLC circuit with an externally controllable capacitance. The diode and antenna coupling strip dimensions are therefore selected so that at the center of the diode reactance range the overall array reactance is zero. To first order, this means that the reactance of the grid array ( $\sim \omega L$ ) is chosen to balance the capacitance of the varactor diode ( $\sim -1/\omega C$ ) at approximately zero bias. The capacitance of the optimum varactor diode element will be

determined in the following Section. This will then allow the strip array design to be established through scaling of the inductance calculations illustrated in **Fig. 3.16**

The variation in the normalized diode reactance that occurs during biasing will then give the maximum rotation about a Smith Chart and hence the maximum reflection phase shift. It has also been pointed out by **Lam et al. (Ref. 2.13)** that the resultant phase shift can be significantly enhanced if *two* grids are utilized in series separated by a quarter wavelength. It has been shown that a change of  $\pm 107\Omega$  (the wave impedance of the GaAs substrate) in the grid reactance can produce an almost linear variation in reflection phase over a range of  $360^\circ$ . In this situation, the series resistance of the diode primarily determines the insertion loss. **Lam et al.** assumed a series resistance of  $10\Omega$  that resulted in a calculated 2.7dB loss. They also indicated that diodes with a series resistance of  $5\Omega$  would reduce this loss to 1.4dB. In later Sections *IR&T* will describe the anti-series biased varactor diode configuration suggested by **Sjogren (Ref. 2.14)** which should significantly reduce the series resistance and thereby produce even lower insertion losses.

**(b) The Varactor Diode Structure and MBE Growth Specifications**

Let us consider some of the issues that are important in the design of the optimum nonlinear element for beam steering arrays. As mentioned earlier the nonlinear element utilized in the arrays will be some form of varactor diode. The array will then consist of diode-loaded metal strips whose equivalent impedance is that of a series RLC circuit with *externally controllable capacitance*. The diode and strip dimensions are selected so that at the center of the diode reactance range the array reactance is zero. A given change in normalized diode reactance will then give the maximum rotation about a Smith Chart and hence the maximum reflection phase shift. One of the important issues is to determine the epitaxial (MBE – molecular beam epitaxy) growth profile that will provide the required C-V characteristic with minimal conduction current over the bias voltage range.

A typical varactor diode consists of *three* layers as illustrated in **Fig. 3.17**:

- (1) a metallic layer that forms the Schottky contact,
- (2) a moderately doped n region which forms the voltage dependent capacitance required

for operation, and

- (3) a heavily doped  $n^+$  region which is employed to provide a low resistance Ohmic contact formed during the array fabrication process.

The one dimensional Poisson's equation is given by

$$\frac{\partial^2 V}{\partial x^2} = -qN/\epsilon_s, \text{ where } N \text{ is the generalized doping distribution}$$

given by  $N = Bx^m$  for  $x \geq 0$  and  $\epsilon_s$  is the permittivity

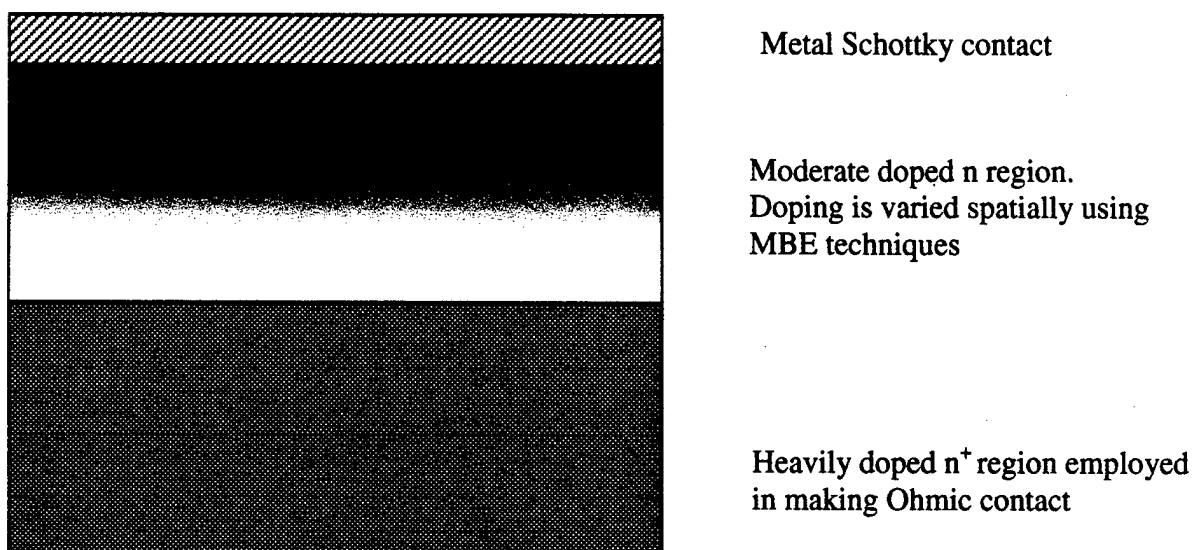


**Figure 3.17** Schematic illustrating basic doping structure for a varactor diode

For  $m = 0$  we have the one sided abrupt junction. For  $m = 1$ , the doping profile corresponds to a one-sided linearly graded case. For  $m < 0$ , the device is called a "hyper-abrupt" junction which can be created through an epitaxial growth process or ion implantation.

The differential capacitance,  $C$  and depletion-layer width  $W$  can be determined through integration of Poisson's equation with the boundary conditions. [ $V(x=0) = 0$  and  $V(x=W) = V + V_{bi}$ , where  $W$  is the depletion-layer width,  $V$  the applied voltage and  $V_{bi}$  the built in voltage]. This leads to



$$W = [\epsilon_s (m+2)(V+V_{bi})(qB)^{-1}]^{1/(m+2)}$$

$$C = [qB(\epsilon_s)^{m+1} \{(m+2)(V+V_{bi})\}^{-1}]^{1/(m+2)}$$

$$\propto (V+V_{bi})^{-s}, \text{ where } s = 1/(m+2)$$

One important parameter in characterizing the varactor is the sensitivity  $s(V)$  defined above. The larger  $s$ , the larger will be the capacitance variation with bias voltage. For a linearly graded junction  $s = 1/3$ ; for abrupt junctions  $s = 1/2$  and for hyper-abrupt junctions with  $m = -1, -3/2$  or  $-5/3$ , the value of  $s$  is 1, 2 or 3. The capacitance voltage relationships for these junction diodes are shown in **Fig. 3.18b** together with their equivalent doping profiles (**Fig. 3.18a**). As expected, the hyper-abrupt junction has the highest sensitivity and gives rise to the *largest capacitance variation* for a given voltage.

As can be seen from the above, the optimum doping profile for a varactor is that of the hyper-abrupt diode, such that  $N = Bx^m$  where  $m$  is less than zero. Therefore, **IR&T** has studied several specific hyper-abrupt junction doping profiles and their resultant C-V characteristic.

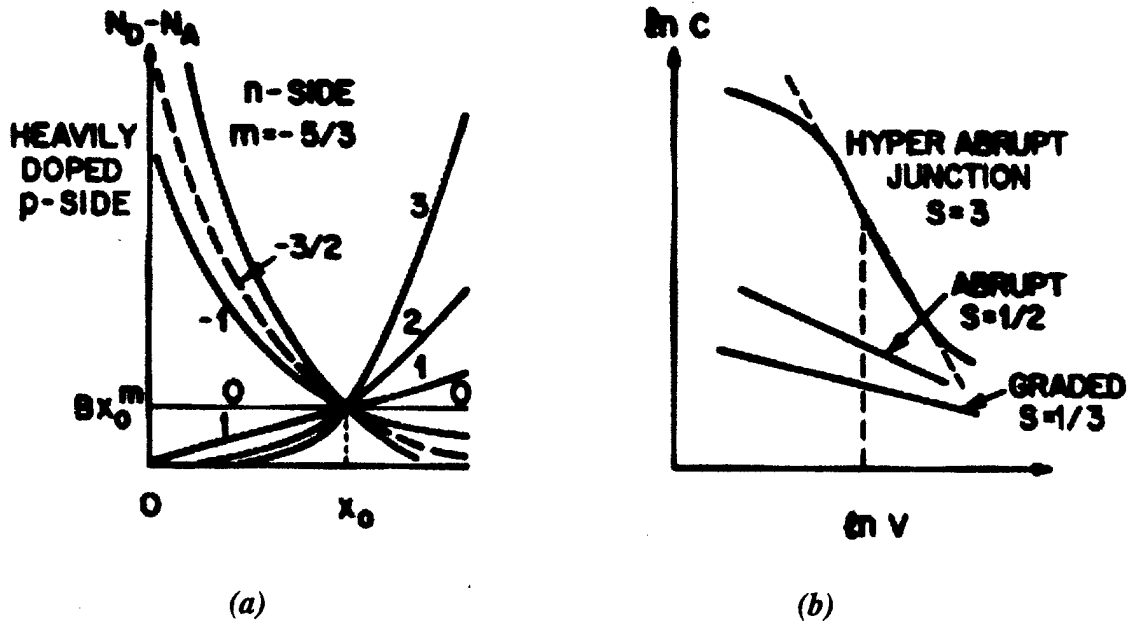


**Figure 3.18** Doping profiles (a) and resultant capacitance voltage relationships (b) for linear, abrupt and hyper-abrupt junctions. (After Sze Ref. 3.6)

In the following, we analyze the most practical doping profiles and obtain their C-V characteristic via device simulations. Here we should mention that the doping profiles investigated at this stage focus on modifications of the important moderately doped n region. **Figure 3.19** shows two distinct doping profiles ( $x=0$  is located at the metallic Schottky contact),

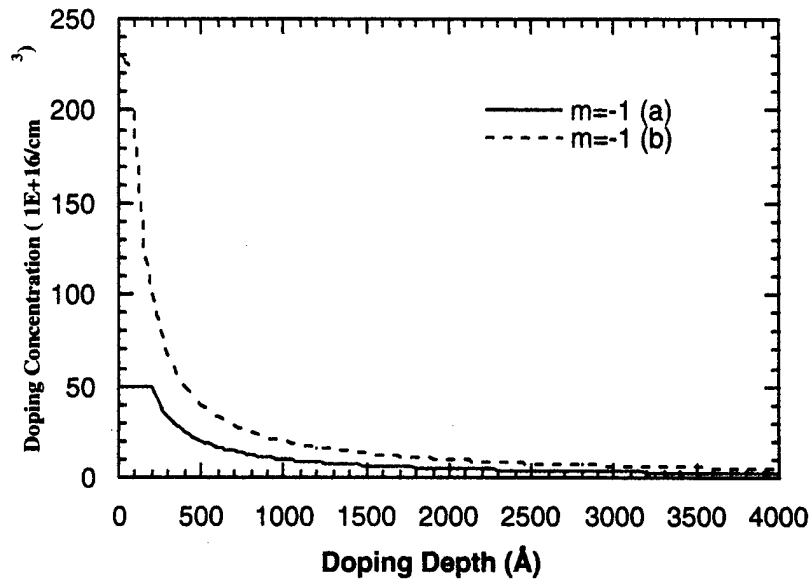


**Figure 3.19** Doping profiles adopted to calculate the resultant C-V curves illustrated in Figure 3.20.

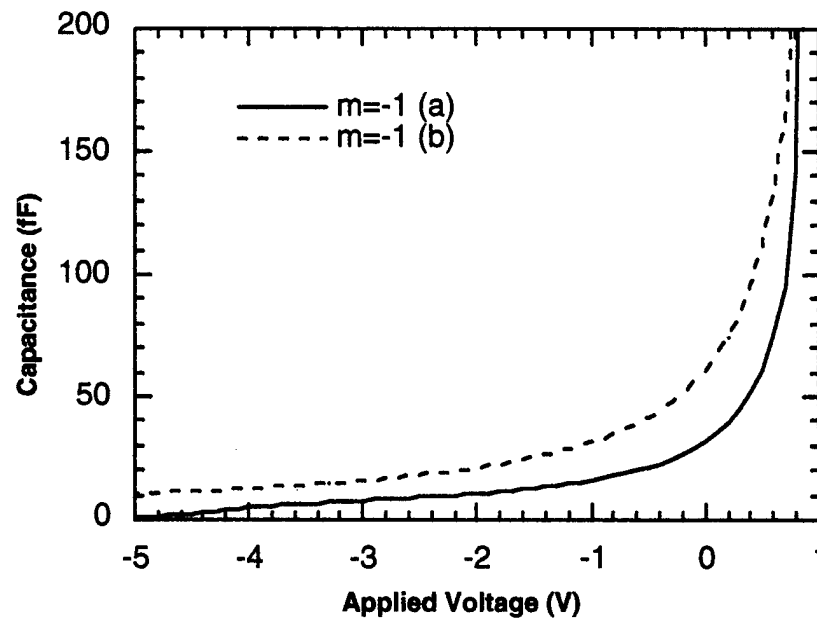


**Figure 3.20** Resultant C-V characteristics calculated using the doping profiles illustrated in Fig. 3.19.

both which maintain the parameter  $m = -1$  fixed. Profile (b) starts with 100Å of heavily doped GaAs:  $n=2.0 \times 10^{18} \text{ cm}^{-3}$ , which is then allowed to decay away from the Schottky contact as  $x^{-1}$ . Profile (a) starts with 200Å of moderately doped region:  $n= 5.0 \times 10^{17} \text{ cm}^{-3}$ , which also is allowed to decay as  $x^{-1}$ . The resultant C-V characteristics are shown in **Figure 3.20**. As can be seen, profile (a) provides more dynamic range in the C-V characteristics (i.e. more non-linearity) than profile (b). Since profile (b) is more highly doped than profile (a), electrical breakdown probably occurs before the hyper-abrupt region is totally depleted. **Figure 3.21** shows doping profile (a) in comparison with a new profile (c). Profile (c) has the same initial doping density (200Å;  $n= 5.0 \times 10^{17} \text{ cm}^{-3}$ ). However,  $m = -3/2$  is adopted which results in a sharper decay in the doping profile. It can be seen in **Figure 3.22** that, as expected, the  $m = -3/2$  doping profile provides a higher device non-linearity than  $m = -1$ . It should be pointed out here that the capacitance shown in the various Figures are calculated assuming a device area of  $25 \mu\text{m}^2$ .

In practice, the ideal hyper-abrupt profile can only be approximated using a "staircase" doping structure. The accuracy of this approximation is dependent on the "fineness" of the staircase utilized during the MBE growth which is directly correlated to cost. A high doping within the staircase is extremely desirable in order to reduce the undepleted region resistance and to maximize power handling capability. However, the doping must not be so high that electrical breakdown occurs before the hyper-abrupt region is totally depleted. The above study indicates that the optimum doping profile is given by **Figure 3.21** with a density decay of  $m = -3/2$ .

Major concerns with the hyper-abrupt varactor design are those associated with thermionic current in forward bias and tunneling current in reverse bias. A high doping close to the surface cannot provide a potential barrier to thermionic emission under forward bias because the electric field associated with this doping appears only across a short distance and therefore integrates to only a small potential. One possible solution is that utilized by Sjogren (**Ref. 2.14**) where a wide bandgap "barrier" layer is added between the aluminum and moderate doping layers. This barrier then suppresses the thermionic and tunneling currents. However, there are also potential disadvantages to adding a barrier layer such as AlGaAs. For example, the lower dielectric constant associated with AlGaAs could lead to a possible lowering of the maximum

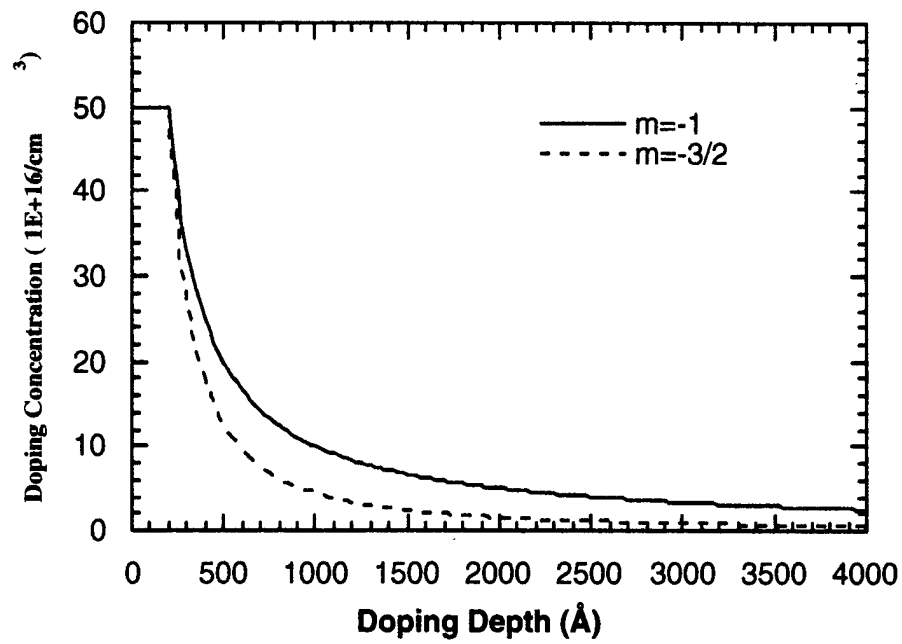


**Figure 3.21** Doping profiles adopted to calculate the resultant C-V curves illustrated in Figure 3.22.

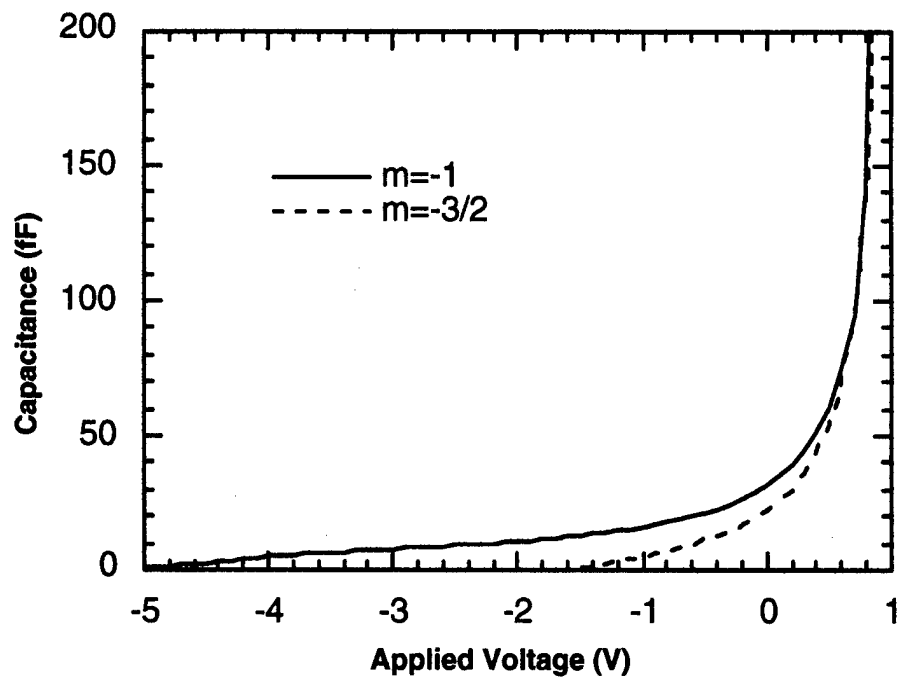


**Figure 3.22** Resultant C-V characteristics calculated using the doping profiles illustrated in Fig.3.21.

attainable capacitance. In Sjogren's experiment,  $\text{Al}_{0.5}\text{Ga}_{0.5}\text{As}$  compound was used as a "barrier" layer. We propose an alternate solution that uses a lower concentration of Al. Study has shown that, for a  $\text{Al}_x\text{Ga}_{1-x}\text{As}$  compound, when  $x > 0.45$ , further increases in the Al concentration do not increase the bandgap voltage. However, increases in the Al concentration will continue to decrease the dielectric constant and therefore reduce  $C_{\text{max}}$ . It is therefore proposed to use a lower Al concentration, such as  $\text{Al}_{0.3}\text{Ga}_{0.7}\text{As}$ , which will significantly increase the breakdown voltage but only modestly affect the  $C_{\text{max}}$ .

As can be seen from the above analysis, a device with an active area of  $25 \mu\text{m}^2$  with a doping profile similar to that illustrated in **Fig. 3.21**, with  $m = -3/2$ , possesses a mid-range capacitance of approximately 30 fF. For 94 GHz this is equivalent to a reactance of  $56\Omega$ . If we choose this point as the center of the bias range, then, as described earlier, the vertical inductive strip dimension must be selected so that the total array reactance is zero. It can be shown that to counterbalance the 30 fF capacitive reactance approximately 95 pH inductance is required ( $\omega L = 56\Omega$  at 94 GHz for an inductance of 95 pH). As illustrated in **Fig. 3.16**, a vertical strip width of  $40 \mu\text{m}$  with a  $300 \mu\text{m}$  line separation would produce an inductance  $\sim 95 \text{ pH}$ . The conclusion, therefore, is that the optimum non-linear element for the monolithic beam steering array is a modified hyperabrupt Schottky varactor diode with a doping profile close to that illustrated in **Fig. 3.21** ( $m = -3/2$ ) as described above. In addition, a thin layer  $\sim 200\text{\AA}$  of  $\text{Al}_{0.3}\text{Ga}_{0.7}\text{As}$  will be grown using molecular beam epitaxy and placed between the metal gate and the moderately doped GaAs region. This serves to significantly increase the breakdown voltage. Finally, a thick layer ( $\sim 1 \mu\text{m}$ ) of heavily doped  $n^+$  GaAs is employed to provide a low resistance "Ohmic contact" formed during the array fabrication process. The antenna grid separation will be  $\sim 300 \mu\text{m}$  (to prevent beam diffraction) and the vertical strip width will be  $\sim 40 \mu\text{m}$ . The bias line width will be greater than  $100 \mu\text{m}$ . We believe, this design will give us a good starting point. However, it should be stressed that at millimeter-wave frequencies, empirical data and experimental verification are always essential components to success. The proposed MBE growth profile utilizing a staircase approximation to **Fig. 3.21** is illustrated below in **Fig 3.23**. Details regarding the antenna grid design, etc. will be described in a following section where the necessary masks and fabrication techniques are outlined. The next Section describes the role that

the proposed anti-series diode can play in reduction of insertion loss alluded to earlier.

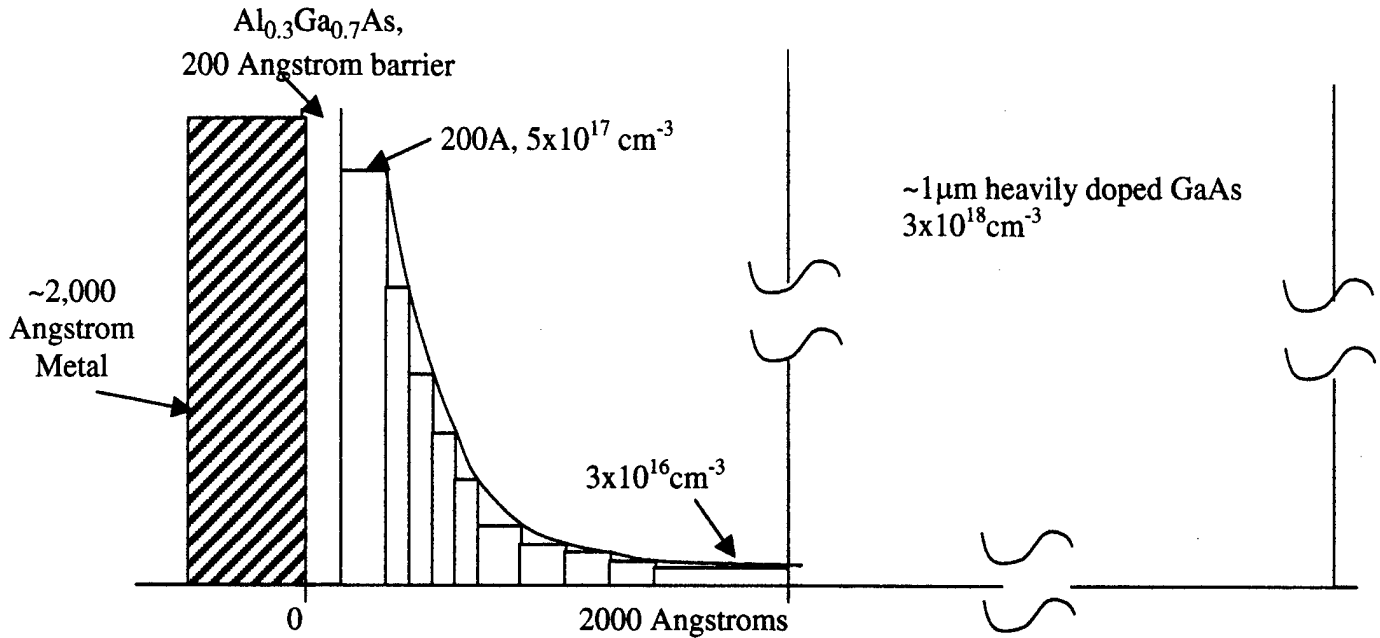


**Figure 3.23** Molecular beam epitaxial growth profile for stair-case approximation to hyperabrupt varactor ( $m=-3/2$ ) diode. Doping starts at  $5 \times 10^{17} \text{ cm}^{-3}$  in a 200 Angstrom step which is followed by a series of 100 Angstrom steps down to a doping of  $3 \times 10^{16} \text{ cm}^{-3}$ . The total doping region including the initial 200 Angstrom barrier is 2000 Angstroms.

### (c) The Anti-series Diode

*IR&T* has developed and demonstrated the advantages of a *back-to-back* configuration for diode array frequency multiplication. A similar concept has been proposed by L. Sjogren (Ref. 2.14) for beam-steering applications : it has been named the "anti-series biased diode" or ABD. One potential limitation to the application of conventional varactor diode arrays for beam steering is the associated series resistance created by the so-called Ohmic contact. This series resistance can be a source of significant RF loss in an electronically steerable antenna. The anti-series biased diode (ABD) employs an anti-series or back-to-back diode configuration which offers the potential for a very low diode series resistance by effectively eliminating the Ohmic contact from the RF path.

In frequency multipliers the *back-to-back* configuration results in natural tripler action and lower series resistance. However, the capacitance of the structure is reduced by at least a factor of two. *IR&T* has direct experience with fabrication and operation of so-called back-

to-back BNN diodes for frequency multiplication. The following provides a summary of *IR&T's* experience in this area.

One of the most successful methods of generating millimeter-wave radiation at higher frequencies has been the use of frequency multiplication or harmonic generation. However, the use of a single multiplier element mounted in a waveguide inherently limits the available output power. This arises because the physical contact area necessary using varactor diodes is extremely small typically having diameters of from 0.1 - 1  $\mu\text{m}$ . This small area generally restricts the maximum allowable pump power to < 100 mW, otherwise the diode will either burn out or breakdown electrically. In addition, the maximum multiplier efficiency is generally obtained at much lower pump powers of ~ 5-10 mW. These limitations have motivated efforts to develop monolithic *multiplier* arrays (Refs. 2.13, 3.7). This approach is attractive because the antennae and nonlinear devices are monolithically integrated into a 2-D array incorporating as many devices as appropriate for the available pump power. This approach, where the nonlinear element and antenna structure are produced monolithically, also has obvious potential for low fabrication costs and high reliability. The concept is illustrated in Fig. 3.24. As noted earlier the concept of monolithic diode arrays has broad application to multipliers, phase shifters, beam-steering, polarization and power modulation

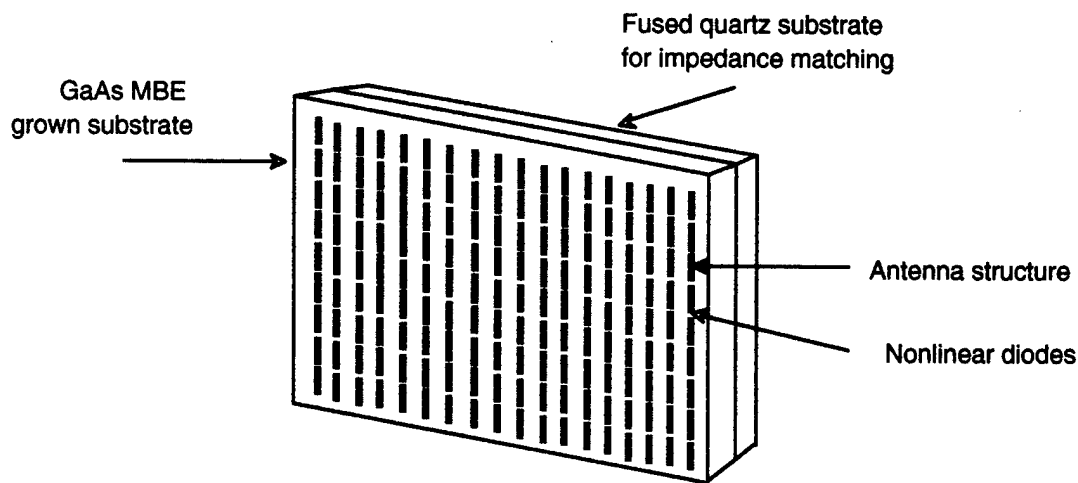


**Figure 3.24** Schematic illustrating concept of a 2-D multiplier array. The array consists of hundreds of non-linear diode elements combined monolithically with their antennae. A second quartz substrate is utilized for impedance matching in a manner analogous to an anti-reflection coating

In a similar manner to the proposed beam-steering array the doping requirements of the chosen nonlinear diode are transferred to a GaAs wafer through molecular beam epitaxial growth. On top of the epitaxial growth a metallic Schottky contact layer is defined, either through MBE growth and subsequent wet etching, or through evaporation. The remaining metallic pattern serves as the Schottky contact, as well as the antenna array which couples the pump and tripled radiation in and out of the diode. The active diode sites are defined through proton implantation that "destroys" surrounding GaAs material and leaves the diode area untouched. Since the GaAs substrate possesses a large dielectric constant, it is backed with a fused quartz substrate of suitable thickness. This acts as an "anti-reflection" coating or quasi-optical impedance match for the emerging tripled radiation. The input pump radiation can be coupled to the array substrate in a variety of ways : through fundamental waveguide, overmoded guide and finally through free space. The most appropriate method depends on the available pump power and the frequency of operation. Multi-Watt level *pulsed* output powers have already been demonstrated in research studies at  $\sim 90$  GHz (Ref. 3.7). In addition, *IR&T* has demonstrated an efficient CW 180 GHz, low-power 60 mW quasi-optical array for NASA remote sensing/astrophysical applications (Ref. 3.8).

**Figure 3.25** illustrates the MBE growth pattern for the BNN diodes used by *IR&T* in the above work at 180 GHz. It should be noted that this growth structure is more complicated than anticipated for the beam-steering array. The heterojunction barrier was chosen to be  $\text{Al}_{0.5}\text{Ga}_{0.5}\text{As}$  which has a barrier height of 1.2 volts relative to the aluminum. The barrier height relative to GaAs is 0.4 V. A moderate thickness of 200 Å was selected for the barrier in order to provide additional resistance to breakdown. In order to reduce the overall series resistance to appropriate levels a doping of  $1 \times 10^{17} \text{ cm}^{-3}$  was chosen for the GaAs drift region. A 30 Å layer of intrinsic GaAs serves as a spacer between the barrier and the Si  $\delta$ -sheet doping. The primary purpose of the sheet doping in the back-to-back BNN is to shift the C-V characteristics so that the capacitance at zero bias ( $C_0$ ) is a maximum. *IR&T* specified a sheet doping of  $1.8 \times 10^{12} \text{ cm}^{-2}$ . The GaAs drift region is followed by a heavily doped region ( $5 \times 10^{18} \text{ cm}^{-3}$ ) which serves as a highly conducting electrode for the back-to-back configuration.



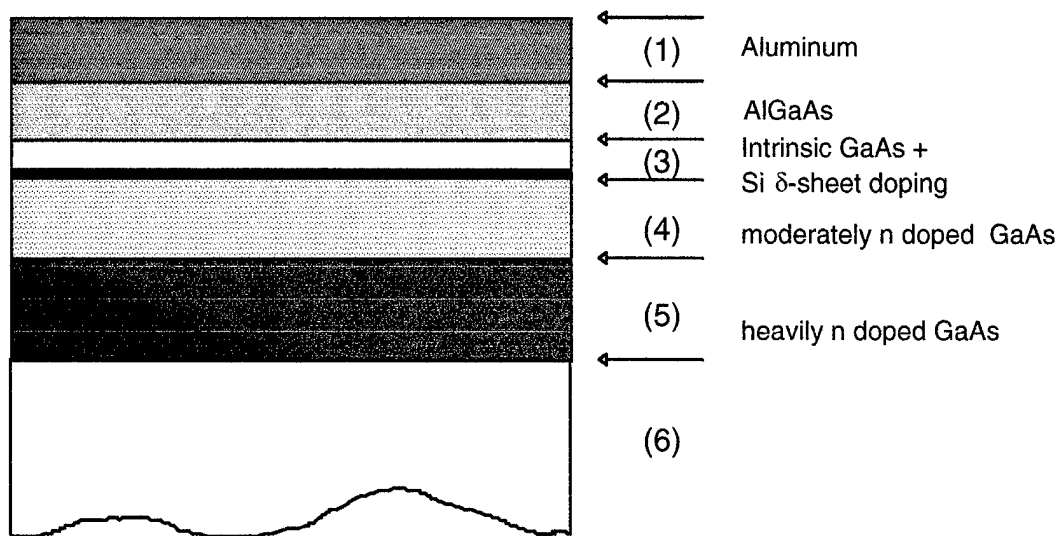


**Figure 3.25** Molecular beam epitaxial (MBE) growth structure for the BNN tripler diode.

A unit cell of the final fabricated BNN diode array is illustrated in **Fig. 3.26**. The fabrication was performed by **Dr. Tony Peebles (P.I., IR&T)** using facilities at the Materials Device Laboratory located at the Jet Propulsion Laboratory, Pasadena. During the follow-on

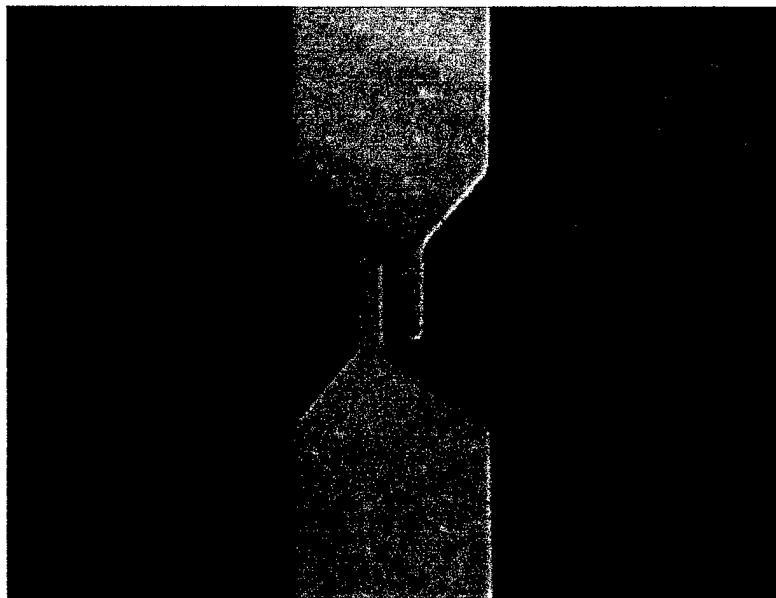


**Figure 3.26** Photograph of unit cell of fabricated BNN tripler diode array.

BMDO Phase II Program it is planned to utilize a similar fabrication facility (The Nano-

electronics Laboratory) at the University of California Los Angeles. The aluminum antennae are  $20\text{ }\mu\text{m}$  wide strips that taper down to fingers that are  $2.5\text{ }\mu\text{m}$  wide and separated by  $1.5\text{ }\mu\text{m}$ . The BNN diode occupies the region between the fingers. Individual array elements are separated by  $200\text{ }\mu\text{m}$ . The processed array was  $\sim 3\text{cm}$  in diameter and contained thousands of diodes. The uniformity and yield were excellent: **Figure 3.27** illustrates an area of the processed array indicating about 70 diodes. Monolithic arrays are well-suited to high-power generation (both pulsed and CW) since the incident power per diode remains low. It should also be stressed that production of such arrays involves extremely low fabrication costs and provides high reliability.

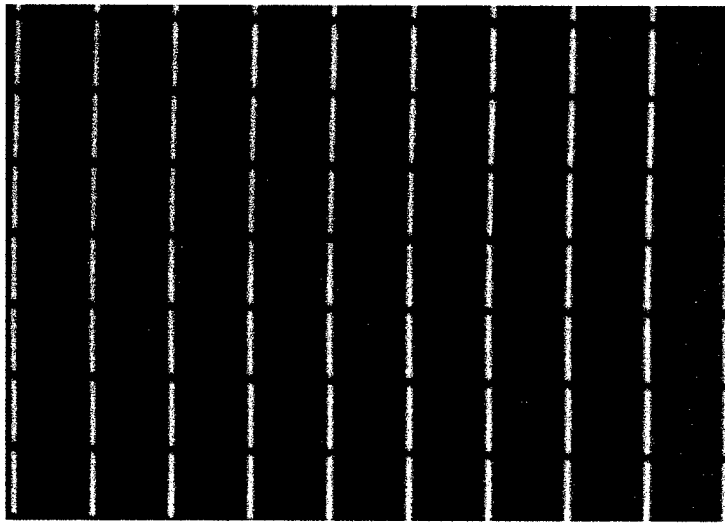


**Figure 3.27** Photograph of portion of fabricated diode multiplier array illustrating approximately 70 diode sites together with aluminum coupling antenna

**Figure 3.28** illustrates the measured capacitance-voltage characteristics for a single back-to-back BNN diode similar to that illustrated in **Fig. 3.26**. As can be seen measured characteristics are symmetrical about zero applied voltage. The applied pump radiation then rf biases the diode and due to the non-linearity generates large harmonic components that are re-radiated. Since the C-V characteristics are symmetrical even harmonics cancel, and the array produces only radiation at odd harmonics. **When unbiased the back-to-back BNN is, therefore, an efficient tripler that requires no idler circuit for the second harmonic.**

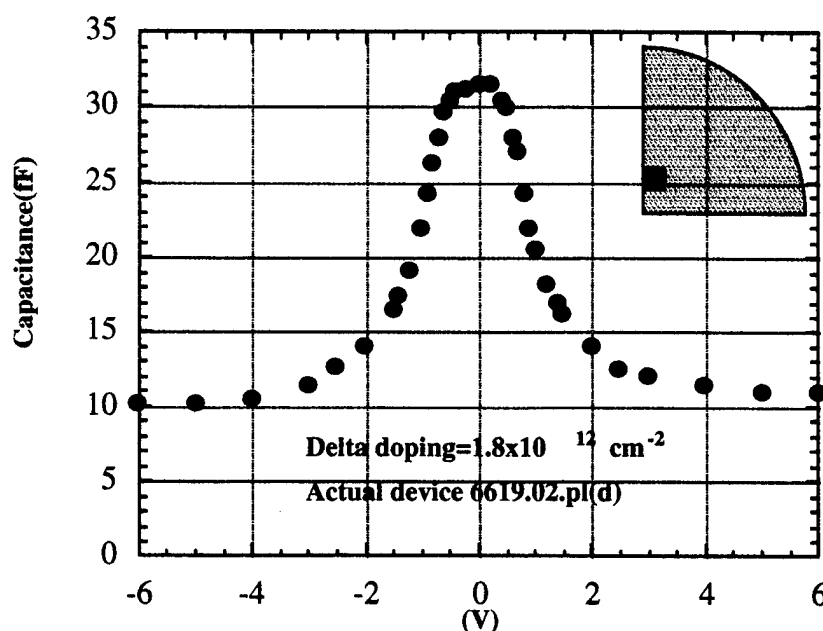


**Figure 3.28** C-V characteristics of back-to-back BNN diode similar to that shown in Fig.3.25

However, if the device is DC biased to  $\sim +1.5$  Volts then the efficiency of generating *tripled* radiation drops drastically. The application of a periodic square wave voltage train would, therefore, effectively switch the generated tripled radiation on and off. *The tripling array can, therefore, with a novel, but simple, modification be used to switch the output on and off with high contrast ratios and at very high rates.* This capability could be utilized for both short range pulsed radar and communication systems.

To summarize *IR&T's* experience with monolithic multiplier diode arrays: the novel use of back-to-back diodes has resulted in efficient generation of tripled radiation and led to reduced series resistance and a simple passive multiplier unit capable of handling large input powers. Application of a low, pulsed, bias voltage can be utilized for rapid modulation control. Let us now return to consideration of the anti-series biased diode (ABD) concept suitable for beam-steering.

The anti-series biased diode (ABD) is similar in many ways to the back-to-back diode concept utilized by *IR&T* for frequency multiplication. The ABD makes it possible to achieve low series resistance while still maintaining the full capacitance range necessary for beam steering. Note in the unbiased frequency multiplier the back-to-back configuration results

in a concomitant reduction in the capacitance. In the ABD this is avoided through the insertion of a cathode contact in conjunction with the back-to-back structure. This concept proposed by Sjogren (Ref. 2.14) can therefore significantly reduce RF losses and make the beam-steering arrays a practical reality. The concept is illustrated in Fig. 3.29 (b). The cathode contact (through the bias lines) allows the diodes to be biased for control. However the RF current flow does not interact with this Ohmic contact : the RF current flows between the thick heavily doped  $n^+$  layer discussed earlier and the metal Schottky contacts. In contrast, the conventional layout for a normal diode (See Fig. 3.29a) array would require RF current flow through the Ohmic contact resistance resulting in significant loss.

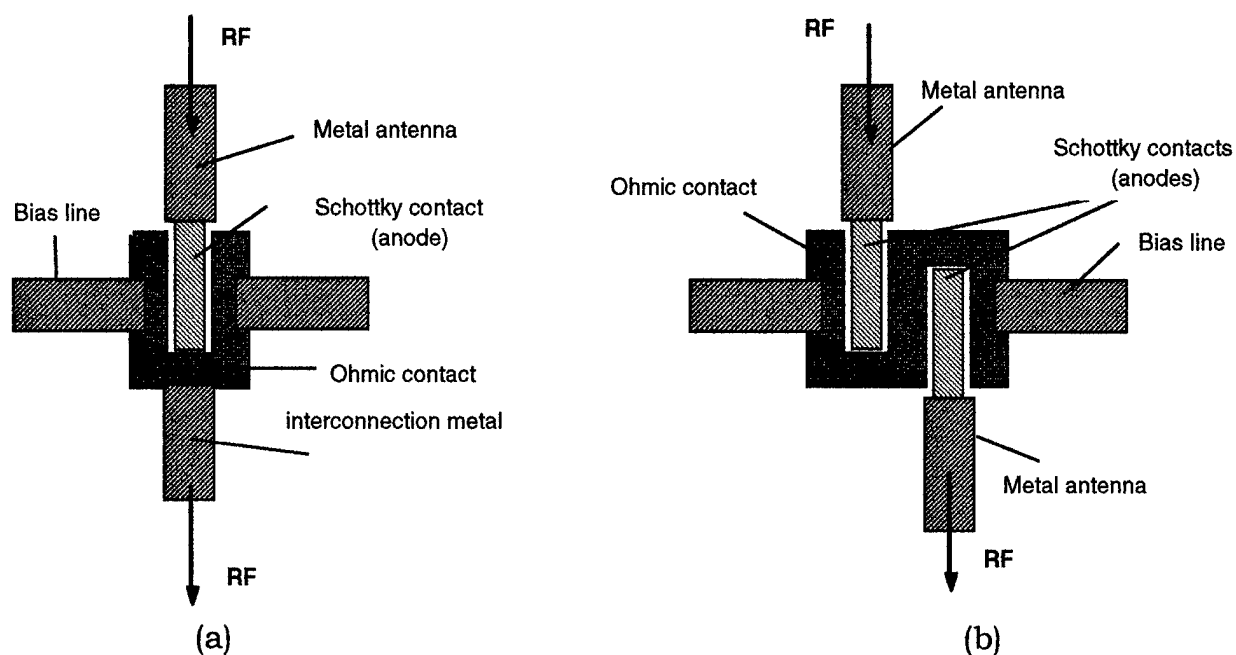


**Figure 3.29** (a) Conventional layout for varactor diode fabrication. (b) Layout for anti-series biased diode. Note that RF current flow is through the heavily doped  $n^+$  layer to the metal antennae. No RF current flows through Ohmic contacts. However, the Ohmic contact allows lower frequency bias voltages to be applied.

As mentioned earlier, L. Sjogren who attempted to demonstrate the advantages during his Ph.D. dissertation (Ref. 2.14) originally suggested the concept of the ABD. ABD arrays were fabricated and utilized as a phase shifter at 120 GHz. However, the arrays did not exhibit the low inherent series resistance expected from the ABD device. This was clearly a result of poor fabrication procedures (excessive wet etching) which resulted in large anode finger resistance.

However, the capability of the ABD concept to produce very low series resistance devices is clear. *IR&T* have concluded that these devices are ideally suited to the beam-steering application. In addition, they simplify fabrication and satisfy the low loss performance requirements. It should be noted that the use of interdigitation of the anode fingers might further improve performance. *IR&T* plans to utilize the ABD hyperabrupt varactor device during the **Phase II Program**. The following section describes the overall mask design and primary fabrication procedures.

**(d) Mask Designs and Fabrication Procedures**

The fabrication process for generation of the monolithic beam-steering diode arrays by *IR&T* is in many ways similar to that employed previously for multiplier arrays. However, since the beam-steering arrays have to be biased, fabrication of good Ohmic contacts will be an important difference. The fabrication process starts with specification of the required MBE growth profile. Molecular beam epitaxial growth on GaAs wafers is performed under ultra high vacuum conditions with molecular beams of the required dopant species. There are now a number of commercial companies that provide MBE growth services (e.g. QED Corporation, New Jersey.). Wafers would be grown under specifications provided by *IR&T*. In order to allow for potential calibration errors, a range of specifications would be provided and a number of wafers fabricated. The cost per wafer during this development stage is not prohibitively expensive – maybe \$2,500 for a three inch diameter GaAs wafer.

After specifying the MBE growth and ordering the wafers, *IR&T* would design and fabricate the required masks. The beam-steering arrays require a maximum of 5 photo-masks for the fabrication. Lay-out for the masks would be performed using the L-Edit Software Program (Tanner Research). This allows final output in the required format (GDSII) for fabrication of the masks by commercial companies such as Align-Rite. The major steps in the fabrication process are illustrated in **Fig. 3.30** where the various masks are schematically illustrated.

**Mask 1** is utilized to define the Ohmic contact region illustrated in dark gray in the Figure. The rectangular areas in the corners of the unit cell are test and wire-bond pads for biasing – it is possible for these to also be fabricated by simple metallization. The MBE grown GaAs wafer is delivered with a top layer of ~2,000 Angstrom of aluminum. This ensures a clean

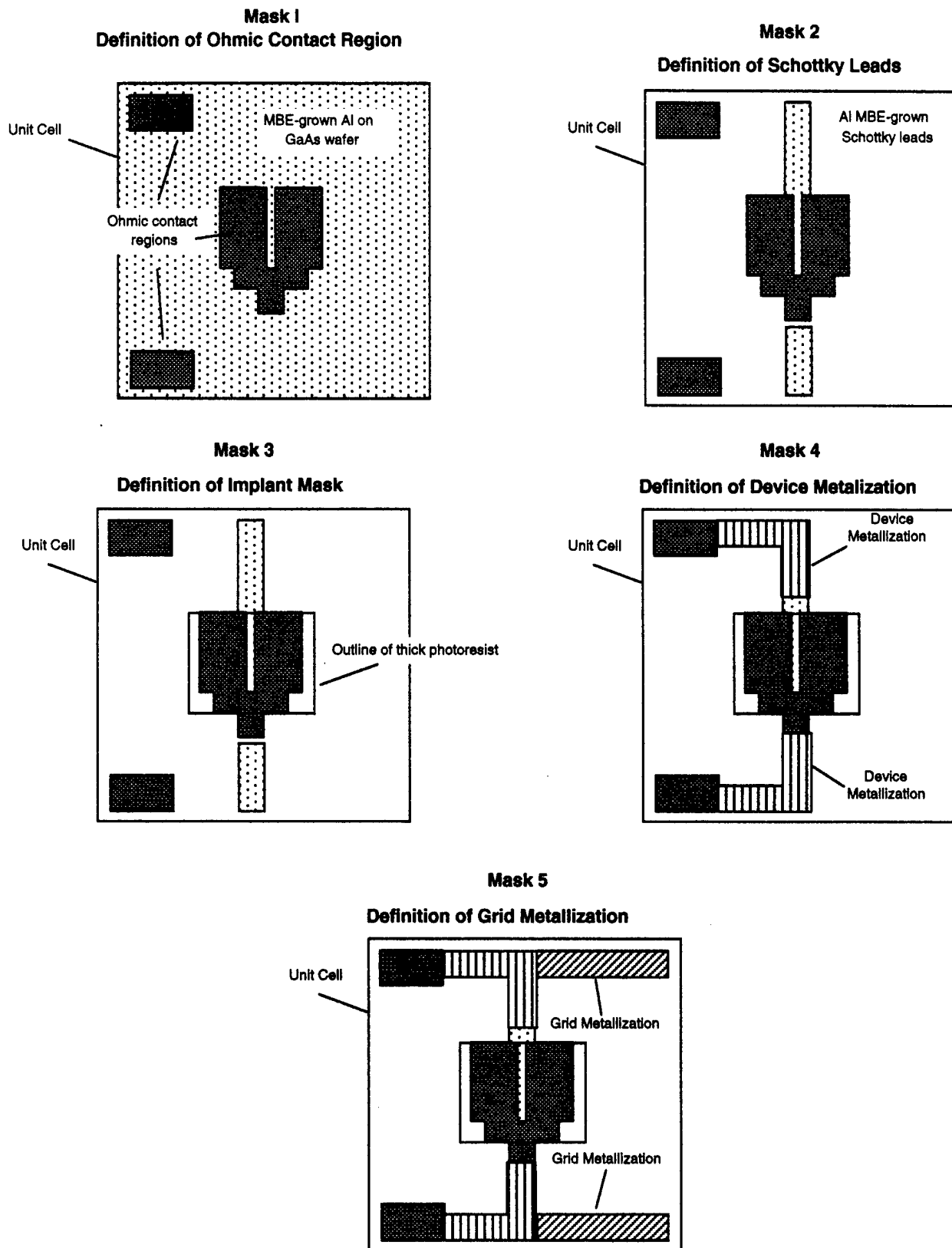


**Figure 3.30** Schematic illustrating the various photo-masks required for fabrication of beam-steering arrays.

Schottky contact. This mask is the so-called self-align mask, since the Ohmic contacts and the diode finger region are self-aligned with each other. The aluminum and top layer of GaAs that occupy the dark gray areas are etched away. Simple wet etching techniques are employed. The aluminum is first removed using hot Transene-D etchant (basically phosphoric acid). The GaAs is then etched down to the heavily doped n+ region using a mixture of de-ionized water, sulfuric acid and hydrogen peroxide. The active diode region lies along the thin finger extending into the Ohmic contact region. After completing the etching of the aluminum and GaAs, Ohmic contact metal (AuGe/Ni/Au) is then deposited. The photo-resist that protects the remainder of the region is then removed to leave Ohmic metal only in the dark gray areas illustrated in Fig. 3.30.

**Mask 2** defines the Schottky contact region. The photo-resist protects the aluminum Schottky diode contact region together with a small strip adjacent to the diode region. Wet etching of the aluminum is then performed using Transene-D etchant and afterward the Photo-resist removed.

**Mask 3** is utilized to define the regions that will remain as active diode material. The mask defines a region where very thick (~7 microns) photo-resist (Hoechst AZP4620) is deposited. This serves to protect the region during proton implantation at a variety of energies ranging from 80kV to as high as 200kV. The different energies penetrate to different depths and "destroy" or isolate those regions. The thick photo-resist does an excellent job of protecting the diode regions. *IR&T* used the same technique during fabrication of the multiplier arrays. Test devices were also patterned to check the effectiveness of the isolation process with positive results. Similar test devices would be fabricated for the beam-steering arrays to confirm the effectiveness of the implantation. The thick photo-resist process has the important advantage of simplicity with trivial mask alignment requirements.

**Mask 4** defines regions specified for device metallization. Metal strips are defined to connect both sides of the diode to the test pads. A lift-off technique is adopted here where photoresist is deposited over the entire wafer and then lifted off in the regions that require metallization. This is followed by metallization through evaporation of layers of chrome and then gold. After deposition the photo-resist is then simply removed. **Mask 5** similarly defines the grid metallization necessary to complete the grid structure necessary for biasing and antennae.

Again a lift-off technique is employed and chrome and gold deposited. After this final metallization the array is complete. *IR&T* believes it should be possible to process complete 3 inch diameter wafers. As can be seen the fabrication primarily requires relatively straightforward wet etching. No dry or plasma etching is required. However, production of good (low series resistance) Ohmic contacts will require care and some additional empirical experimentation to achieve the required outstanding results. However, *IR&T* has confidence that uniform high quality arrays can be routinely produced that will enable the realization of the desired low-loss electronic mirror and thereby an previously unattainable all-weather, surveillance capability.

### 3.3 Conclusions and Future Plans

This SBIR Phase I Program has clearly established feasibility of a radical, new, all-weather, surveillance system suitable for implementation on uninhabited aerial vehicles as well as other platforms. It has long been recognized that operation at mm-wave frequencies allows penetration of clouds, fog, sand, camouflage, etc. thereby extending and complementing existing surveillance capabilities in the visible and infrared spectral regions. However, implementation of a mm-wave, all-weather imaging system possessing adequate spatial resolution has been unavailable to-date due to the required large apertures and associated weight and power limitations. *IR&T* have proposed an innovative solution through development of a *beam-steerable*, sparse-aperture, interferometric imaging approach. Beam-steering is achieved through use of an "electronic mirror" based on a planar array of varactor diodes integrated with antennae and bias lines. Analysis performed during the Phase I Program has confirmed that the proposed approach reduces the required number of sparse-array antennae elements by at least an order of magnitude, thereby reducing weight and power requirements to a level that integration into the Predator, Dark Star or Global Hawk UAVs becomes practical. Predicted performance of the sparse array, mm-wave-imaging system is good to excellent dependent on the severity of the weather conditions. Spatial resolution varies from 1 to 3 m and is dependent on the UAV altitude and assumed size of the sparse array antenna. For example, a system integrated into the Predator UAV flying at an altitude of 3km would have a spatial resolution of ~0.7m, whereas integration into Global Hawk flying at 18.2km would realize a resolution of 2.2m.

The concept of the electronic mirror has been analyzed during the Phase I Program and



preliminary design completed. As described in the main body of the report, the electronic mirror is crucial to realization of the highly desirable all-weather surveillance capability. The Phase I Program has confirmed the validity of the diode array approach. The required fabrication masks have been designed and the MBE growth profile established. The next important task is fabrication and test of the electronic mirror at 94 GHz. This forms the basis of the follow-on Phase II Program. Demonstration of the electronic mirror opens up a huge array of application areas including the all-weather surveillance capability that forms the focus of the current program. During the Phase II Program a large aperture electronic mirror would be fabricated and fully tested. In addition, it would be utilized in a ground-based radiometric imaging system to fully demonstrate imaging performance. Finally, in collaboration with General Atomics, a detailed design of a beam-steerable, sparse-array, all-weather imaging system would be completed to implement such a system on the Predator UAV. A successful program would usher in a new era of surveillance capabilities complementing existing all-night capabilities with a covert, all-weather performance

### References

- 3.1 J.W. Goodman, *Introduction to Fourier Optics*, McGraw-Hill, 1968.
- 3.2 R.J. Mailloux, *Phased array antenna handbook*, Artech House, 1994.
- 3.3 *Microwave Remote Sensing, Vol. 1*, by F. T. Ulaby, R. K. Moore, and A. K. Fung.
- 3.4 M. Kim, R.M. Weikle III, J.B. Hacker and D.B. Rutledge, "Beam Diffraction by a Planar Grid Structure at 93 GHz", 1991 APS Symposium Digest pp. 150-153.
- 3.5 N. Marcuvitz, "Waveguide Handbook", IEE Electromagnetic Waves, Series 21
- 3.6 S.M. Sze, "Physics of Semiconductor Devices" 2nd Ed. Wiley, New York (1981)
- 3.7 H.X. Liu et al., "Monolithic Quasi-optical novel Solid-state Device Tripler Array with 5 Watt output Power at 99 GHz" IEEE Electron Device Lett., 14, 329-331 (1993)
- X-H. Qin, "A Millimeter-wave Monolithic Barrier N-N+ Diode Grid Frequency Doubler", UCLA Electrical Engineering Department M.S. Thesis (1993).
- Also "Millimeter-wave Monolithic Barrier-N-N+ Diode Grid Frequency Doubler" App. Phys. Lett. 62(14) 1650-1652 (1993)
- 3.8 W.A. Peebles & A.L. Peebles, "Development of Terahertz Radiation Sources", Conference Digest of the Int. Conf. on MM and Submm. Waves & Applications, San Diego, Ca. January 1994, SPIE Proceedings 2250, pg. 144- 146. Also see Final Report of NASA SBIR Contract NAS7-1192 entitled "Quasi-optical, Solid-state Multiplier Sources to 3,000 GHz"